POLITECNICO
MILANO 1863

Industrial and Information Engineering School

Master Degree in Engineering Physics

Ultrafast dynamics in 2,6-Dimethylpyridine investigated by sub-20-fs resolved UV pump - XUV probe photoelectron spectroscopy

Advisor:

Mauro Nisoli

Co advisor:

Maurizio Battista Reduzzi

Stefano Severino

Autor:

Edoardo Alberto Boati

Academic Year

2023/2024

Grazie,
a chi c'è sempre stato
e a chi ci sarà sempre
o solo per un atto,
indipendentemente.

Contents

List of Figures

Abstract

The possibility to generate pulses with characteristic durations in the order of few femtoseconds to hundreds of attoseconds (1 as = 10^{-18} s) has allowed impressive advancement in our understanding in many different fields. During the last twenty years and beyond, a great interest has always been focused on the world of molecules. The idea of studying not only the electron dynamics, but being able to access to its characteristic time scale preceding any notable nuclear motion set the beginning of huge efforts to investigate this world.

Many different molecules drove the attentions of these efforts and pyridine is one of these due to its important roles in the UV photodamage of nucleic acids. These studies opened the door to the investigations of pyridine derivatives allowing to understand the effect and the role of different substitute like methyl group with a depth never seen before. 2,6 dimethylpyridine is a perfect example of how the addition of substitute groups can radically change the dynamics of a molecules after UV excitation. This exact case will be explored in the present work through the means of a pump UV and probe XUV experiment.

With the advent of the attosecond technologies it became fundamental to develop solutions to be able to characterize such pulses. Various systems were created (RABBITT, attosecond streak camera and so on), in the present work the results of the temporal reconstruction of the XUV and UV pulses is presented, through the means of an algorithm called STRIPE.

From the pulses reconstruction to their exploitation for the study of the biologically interesting 2,6 dimethylpyridine: the following pages cover the general fundamental steps to perform an experiment in the attosecond framework.

1. Introduction

The present work is organized as follows: in the first chapter 1 an introduction to attosecond science and physics is presented with a digression on the historical evolution of this branch and a focus on the kinds of processes that were allowed to be observed and studied with these new means. The second chapter 2 introduces all the necessary theoretical tools to have a basic general understanding of what this field is based on, therefore representing a more technical approach to the subject. Before the presentation of the work done, the setup used in all the experiments performed is showed in the chapter 3. In chapter 4 the first experimental results and analysis are explained as well as the methodology and tools exploited to obtain them. They concern the reconstruction and characterization through an algorithm called STRIPE of two different pulses, one in the XUV energy range, the other in the UV. This reconstruction is fundamental to provide any data regarding experiments performed in molecules with the aforementioned pulses. The chapter 5 contains the presentation of different kind of results, that is those regarding a UV-pump and XUV-probe experiment on 2,6 dimethylpyridine to study the electronic ultrafast dynamics inside the molecule, showing a perfect example of what attosecond science has enabled us to study and observe.

1.1   Attosecond Science

To understand a physical process it is necessary to have a clear view of its evolution in time. As an example the trajectory of a moving object can be observed through the employment of a camera. Historically this brought to the development of many different solution to try to solve a great diversity of problems and eventually to keep on setting the level of the obtainable precision and resolution higher. Together with this, there was a progress on the type of processes and phenomena we can study and observe, along with a higher level of complexity.
In 1872, the Governor of California Leland Stanford, asked Eadweard Muybridge, a British photographer, to confirm a hypothesis of his: during a horse's gallop, there is a moment when all four legs are off the ground. This was not an easy task, but in 1878 he successfully photographed

a running horse using 24 cameras arranged in parallel along the track (fig.1.1), reaching a resolution of about 1 ms.
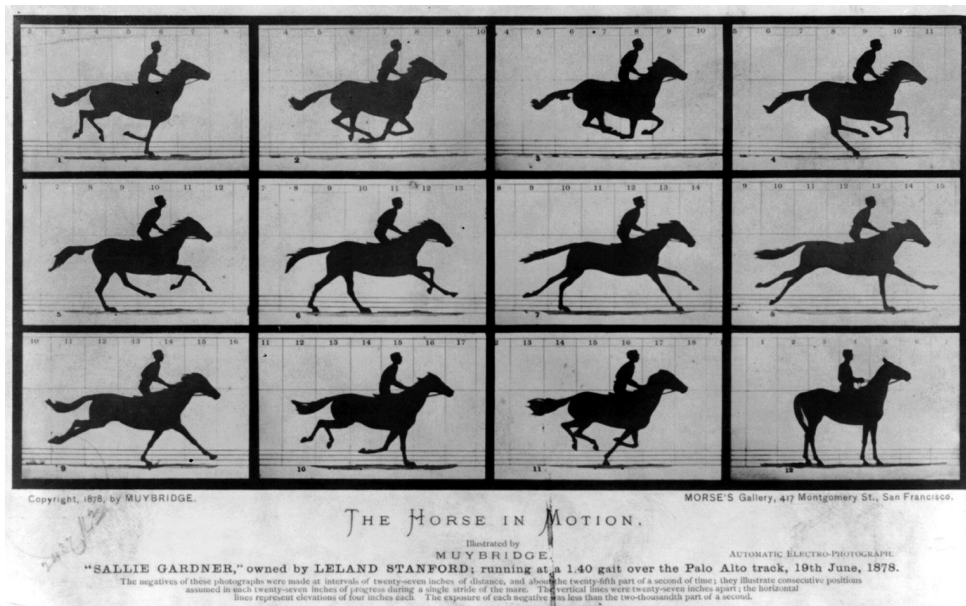
Figure 1.1: Eadweard Muybridge, photo series of a galloping horse, 1878.

About a century later, in 1964, Harold Eugene Edgerton succeeded in taking one of the most famous pictures in history: the exact moment in which a bullet hits an apple (fig.1.2), requiring an exposure of less than 10^{-6} s.
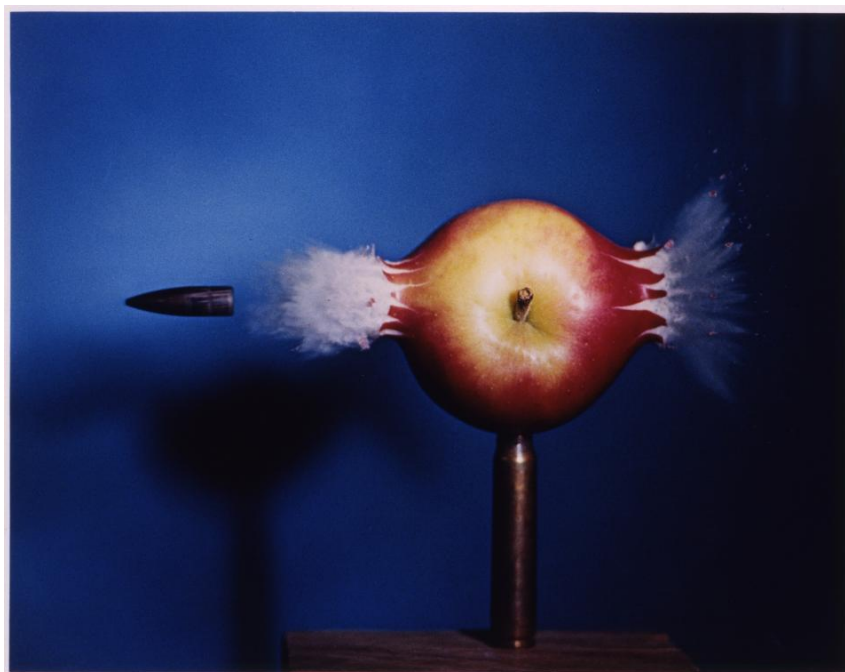
Figure 1.2: Harold Eugene Edgerton, 1864.

Around half a century later attosecond science can reach a timescale resolution that allows to perform measurements and observe dynamics like evolution of the electron motion in a molecule on its natural timescale, that is the one of the attosecond, 10^{-18} s. These kind of dynamics are remarkably faster than those which characterize other phenomena at the nano-scale or smaller: the time scale of the rotational motion of molecules is on the order of picoseconds 10^{-12} s and the vibrational molecular motion on the order of femtoseconds 10^{-15} s (Section 2). Therefore this technology did not just allow a greater resolution on certain phenomena, but it opened the door for the observation of processes that could have never been studied before, since it almost abruptly improved the temporal resolution of time-resolved spectroscopy by two orders of magnitude. In particular the attosecond spectroscopic tools established in the last two decades, together with the development of sophisticated theoretical methods for the interpretation of the experimental outcomes, allowed to unravel and investigate physical processes never observed before, such as the delay in photoemission from atoms and solids, the motion of electrons in molecules after prompt ionization, the temporal evolution of the tunneling process in dielectrics, and many others [8].

1.2 Historical Overview of Attosecond Science

The study of the historical evolution of sciences is undoubtedly a topic of great interest, if only to satisfy curiosity about how we have arrived at today's technological means and knowledge. However, I believe that delving into the discoveries and results that have unfolded over the years, allowing us as a human species to take a small step further into the unknown, is not merely an amusement to satisfy one's curiosity. The exploration of what has preceded us, if one has the interest to do so, can provide a historical awareness that transforms into a general consciousness regarding the subject under study. This awareness can be of enormous importance, not only to have a clear understanding of the current state of the art in science but also to navigate more confidently through all the nuances that a branch of knowledge has to offer, no matter how specific it may be. The combination of scientific knowledge and consciousness offers much more of what is reachable by just one of the two. These are the reasons at the basis of this chapter which purpose is to provide a brief historical reconstruction of the evolution of this powerful and beautiful science.

In 1864, August Toepler extended spark photography, already known as a method for recording rapid motion of macroscopic objects, to study microscopic dynamics. He generated sound waves with a short light spark and subsequently photographed them with a second spark that was delayed electronically with respect to the first one initiating the motion. By taking pictures of the sound wave as a function of the delay time, he obtained a complete history of sound-wave phenomena. This marked the birth of the pump-probe technique [32]. However these were just the first steps of this incredibly powerful technique and to be able to study faster phenomena required some years of research.

Clearly, the evolution of the technology was not linear. There were different big discoveries which brought great steps up in what was and currently is the state of the art of this field. In the following a reconstruction of the main events is reported with a major focus on what are the most important changes, strictly linked to the attosecond science.

1.2.1 1980s - First revolution: laser pulses for pump-probe spectroscopy

The resolving power of pump–probe techniques was limited by the nanosecond duration of light pulses for more than half a century, before laser-based techniques improved it by six orders of magnitude within merely two and a half decades as reported in fig.1.3.
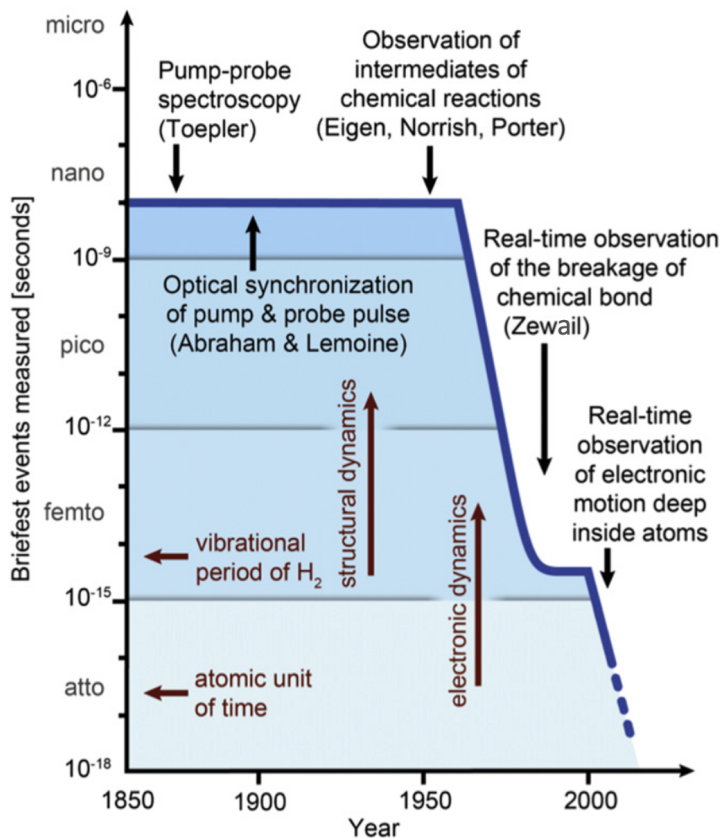
Figure 1.3: Evolution of techniques for real-time observation of microscopic processes [32].

Indeed, in 1967 the Nobel Prize in chemistry was shared between Manfred Eigen and Ronald Norrish together with George Porter for the techniques they developed right after the World War II in the study of chemical dynamics. They were able to study reactions at the sub-millisecond timescale, breaking this limit for the first time [66]. Two and half decades past and during the 1980s Ahmed Zewail conducted a pioneering investigation of fundamental chemical reactions exploiting femtosecond laser pulse generation and measurement techniques permitting real-time observation of the breakage and formation of chemical bonds, therefore the study of dynamic changes in molecular and crystalline structure. These efforts were worth him a Nobel Prize in

chemistry in 1999. This was an absolute revolution in the field and was possible thanks to the invention of the lasers along with nonlinear optical techniques for generating and measuring femtosecond pulses able to reach a duration as short as 6 fs in the mid 80s [17].

Progress in temporal resolution was again slowed down in these years, since the duration of the shortest laser pulses approached the several-femtosecond oscillation period of the lightwave carrying the pulse. This represented a problem without an immediate easy solution since the nJ energy scale of these pulses was insufficient to extend ultrashort-pulse generation to much shorter wavelengths via nonlinear frequency conversion.

1.2.2   1980s-1990s - Second revolution: femtosecond solid-state lasers and high-order harmonics generation

To tackle the problem mentioned above it was necessary to scale the femtosecond pulses from energies in the order of nJ to mJ, so an increase of about 5 orders of magnitude. Three great inventions lay the foundations for this change to come: the broadband solid-state laser medium, titanium-doped sapphire (Ti:Sa) by Peter Moulton [42], self mode locking (referred also as Kerr-lens mode locking, KLM) by Wilson Sibbett and coworkers [55] and chirped-pulse amplification (CPA) by Gerard Mourou (Nobel Prize in physics in 2018) and coworkers [58]. These inventions built the second generation of femtosecond technology through the exploitation of solid-state laser media solving the problem of the low energies that used to characterize the ultra-short pulses.

The problem of the duration of femtosecond laser pulses approaching the oscillation period of the lightwave carrying the pulse is still to be solved. An approach adopted to try to solve the problem was the high-order harmonic generation HHG to create several-cycle pulses in the extreme ultraviolet (XUV). However this attempt at first did not came out as it was hoped, since the solution provided pulses too weak to be measured by standard nonlinear autocorrelation techniques. The introduction of the solid-state Ti:Sa lasers changed the things: from the late 80s to the beginning of the 90s Anne L'Huillier and coworkers demonstrated, in a series of pioneering experiments, the feasibility of extending the generation of coherent radiation from the VIS/IR spectral range (covered by lasers) to several orders of magnitude shorter wavelengths, in

the XUV [36] [38] [34] [35]. This was made possible through the HHG from powerful ultrashort laser pulses from solid-state lasers. This efforts will be worth Anne L'Huillier, Pierre Agostini and Ferenc Krausz the Nobel Prize in physics in 2023.

The second revolution made it possible to perform pump–probe spectroscopy with a resolution that permitted the direct observation of electronic motions for the first time.

1.2.3 1990s - Higher-order dispersion limiting the pulse duration and CEP control

Despite the huge advancements in technologies, the utter exploitation of their potentialities required more work. The laser like the Ti:Sa produced pulses not close to the Fourier-limit imposed by the bandwidth, e.g. the first Kerr-lens-mode-locked (KLM) Ti:Sa laser produced pulses of 60 fs duration that was more than an order of magnitude longer than what was allowed by a bandwidth stretching over 600 - 1100 nm. The limitation was to be found in the employment of the prism sequence for group-delay-dispersion (GDD) control which introduced higher-order dispersion.

Once the problem was understood, research began to find a solution and at the beginning of the 90s many efforts were aimed at developing multilayer mirrors for providing tailored dispersion for shaping the pulse emerging from the mode-locking process in the laser cavity and maintaining at the same time high reflectivity over the required bandwidth. By the late 1992 the first chirped mirrors were produced, even if far from absolving perfectly to their job, since they did not provide any degree of freedom for the GDD adjustment.
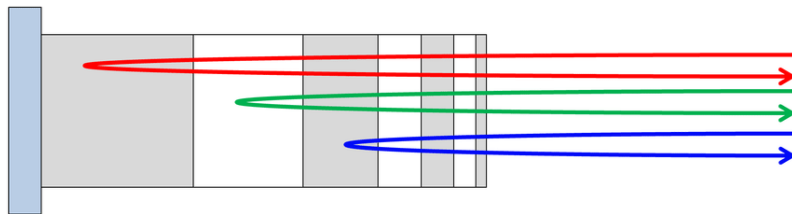
Figure 1.4: Chirped mirror example of operation. Narrow-band wave packets carried at different wavelengths penetrate to different depths before being reflected, as a consequence of a modulation of the multilayer period across the layer stack. The process gives rise to a negative GDD allowing to compensate the chirp of the pulse in input.

In 1993 chirped mirrors (CMs) were successfully exploited in a mirror-dispersion-controlled femtosecond laser (Kerr-lens-mode-locked (KLM), Ti:Sa) by the Ferenc Krausz's group [61]. Mirror-dispersion-controlled Ti:Sa laser technology rapidly entered the sub-10 fs regime and started to outperform any other femtosecond oscillator technology thanks to different others pioneering works like semiconductor saturable absorbers by Ursula Keller [60].

Another fundamental work worth mentioning, especially considering the laboratories in which all the work in the present thesis took place, is the work by Orazio Svelto, Sandro de Silvestri and Mauro Nisoli. They invented a new optical compression technique based on gas-filled hollow-core fibers to broaden spectrally high-energy pulses via self-phase modulation ad subsequently compress them through the CMs [44].

Times were ripe for the isolation of a single cycle of strong laser field, that was indeed achieved, constituting a powerful tool through which study the strong-field - matter interaction. Another problem rose: uncontrolled shifts of the phase of the carrier-wave with respect to the amplitude envelope of the pulse, that is carrier-envelope phase (CEP), led to small variations in the sub-cycle evolution of a few-cycle laser field and might cause significant pulse-to-pulse variations in the evolution of the electron processes triggered and driven by these fields. From 1996 onwards the issue was faced and eventually a solution was found in 2003 by Ferenc Krausz and coworkers who were able to control the attosecond temporal structure of coherent soft X-ray emission produced by the atomic currents [2]. The full control over the CEP came with the work of Theodor Hänsch who developed a frequency-comb technique which was worth a Nobel Prize in physics in 2005 [19].

1.2.4   2000s - First attosecond pulses and their characterization

The first attosecond pulses were demonstrated in 2001 [46] [21]. They reported a temporal characterization of the XUV radiation formed in the HHG process, demonstrating that it could lead to the formation of attosecond pulse trains (APTs) or isolated attosecond pulses (IAPs). Ever since, pulse characterization has been a persistent challenge in attosecond science [5]. The study of fast evolving processes would not be possible without the attosecond technology, but the pump and probe experiments require necessarily the capability to characterize the employed pulses.

The direct application of well established methods for the characterization of femtosecond pulses (VIS/IR range) such as frequency-resolved optical gating (FROG) and spectral phase interferometry for direct electric field reconstruction (SPIDER), to the attosecond XUV regime was not possible. This is due to some challenging factors, mainly the large spectral bandwidth of these pulses, the high photon energies and the low photon flux, therefore entirely new approaches to diagnose bursts of XUV to soft x-ray light therefore had to be devised. In the early 2000s successful schemes were developed, typically involving a nonlinear interaction of a target with both the attosecond pulse and a co-propagating IR fundamental field, and applied to new reconstruction algorithms. In 2002 the reconstruction of attosecond harmonic beating by interference of two-photon transitions (RABBITT) was applied in the weak IR field regime for ATP reconstruction [43] and the streaking schemes [24] in strong field regime. In a RABBITT measurement, interferences between two-color ionization pathways involving different harmonics are used to determine the relative phase of these harmonics while in a streaking measurement, changes to the momentum distribution of photoelectrons are measured as a function of the delay between the XUV pulse and a co-propagating IR field.

The first pump–probe experiments where attosecond pulses were applied to investigate time-dependent electron dynamics were performed in 2002 in particular with an investigation of the lifetime towards Auger decay of core-ionized Kr atoms [15]. From this moment onwards, the experiments that exploited this technology became more popular. At the early stages it was confirmed the ability of attosecond pump–probe spectroscopy to determine atomic properties such as excited state lifetimes by means of measurements in the time domain, finding results in agreement with what could be obtained through a frequency domain investigation. Subsequently, in mid 2000s early 2010s, attosecond pump–probe spectroscopy was applied to explore questions that cannot be answered in the frequency domain, such as the nature of ionization processes in the strong field regime [64], and the question whether or not single-photon ionization from different atomic or molecular orbitals occurs simultaneously or with a small relative delay [54] [30].

It is easy to imagine that, along the great progress in ultra-fast technologies and pulses characterization, there were efforts also to improve the laser sources themselves.

As explained above the early development of attosecond science was entirely based on chirped-

pulse amplification-based Ti:Sa technology and during these years received a major impetus with the ability to generate few-cycle pulses with (CEP) stability at high peak intensity [70] [63]. To mention some results made possible by this progress: advent of IAPs in the XUV region [3], improved understanding of the electron's continuum and re-collision dynamics [37] and the underlying quantum trajectories [39], CEP-controlled few-cycles pulses were used in first experiments controlling molecular electron dynamics on attosecond timescales [29].

A second step up came with the ability to generate CEP-stable few-cycle pulses at mid-infrared wavelengths [11] [50]. Such long wavelengths enable a ponderomotive scaling of the strong field interaction due to the much longer excursion of the tunnel-ionized electron [7] and and correspondingly higher kinetic energies upon recollision directly impacting the range of photon energies produced in HHG, since the spectrum has a cut-off that scales with λ^2.

Eventually a third, more recent, important advancement in laser sources was obtained with the development of solid-state, fiber and OPCPA-based systems that combine high peak power with high average power [28] [45] [16] [6]. These systems nowadays permit to conduct experiments at 1–3 orders of magnitude higher repetition rates than the first generation, 1 kHz Ti:Sa systems, meaning the possibility to reach a better signal to noise ratio.

1.2.5 Present

Attosecond science potentiality is huge and to sum up all the applications and branches of research linked to this field would be a really demanding and complex work that is out of the scope of this brief historical reconstruction. To mention some applications: atomic photoionization dynamics are studied by probing the emitted electron making it possible to study how long does it take for an electron to photoionize (Wigner delay), investigation of the ultrafast charge migration and coupled electronic and nuclear dynamics in molecules, issues related to the HHG (increase its efficiency, manipulate the polarization state of the harmonics, high-resolution spectral manipulation over the harmonic spectrum, ...), HHG in plasmas and in solids and so on.

To this purpose it is more useful to directly show one application, that is a pump and probe experiment performed with a UV pump and an XUV probe as reported in the chapter 5. To end this chapter in fig. 1.5 is shown the evolution of the duration of the shortest pulse that could be generated from before the 1970s.
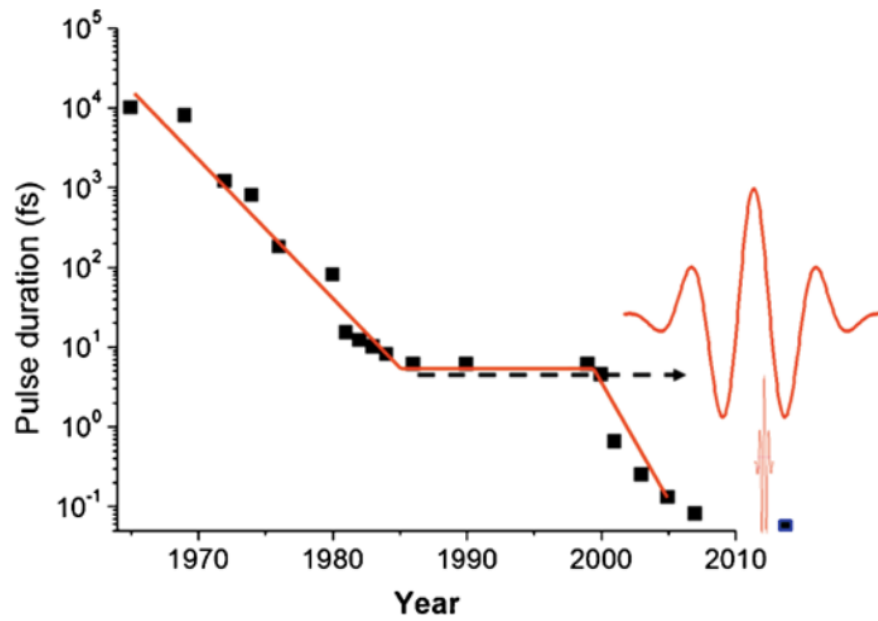
Figure 1.5: The shortest pulse that could be generated as a function of time since mode locking was developed [47].

2. Attosecond Physics Theory

Quantum mechanics tells us that with a simple model we can characterize an atom with a eigenfunction ψ and its electronic distribution can be described as through the function $|\psi|^2 = |u|^2$. The quantum interpretation of the classical motion implies the presence of a wave packet, that is coherent superposition of eigenfunctions. The simplest case we can analyse is:

$$|\psi\rangle = c_1 e^{-i\omega_1 t} |u_1\rangle + c_2 e^{-i\omega_2 t} |u_2\rangle \qquad (2.1)$$

therefore:

$$|\psi|^2 = \psi^* \psi = |c_1|^2 |u_1|^2 + |c_2|^2 |u_2|^2 + 2Re\left\{ c_1^* c_2\, u_1^* u_2\, e^{-i(\omega_2 - \omega_1)t} \right\} \qquad (2.2)$$

obtaining an oscillating term $\omega_2 - \omega_1$, so a periodic modulation of the electronic distribution. Its period can be estimated as:

$$T = \frac{2\pi}{\omega_2 - \omega_1} = \frac{2\pi h}{(\varepsilon_2 - \varepsilon_1)} = \frac{h}{\Delta \varepsilon} \qquad (2.3)$$

Suppose we are dealing with a molecule, it is characterized by different degrees of freedom which describe different physical processes e.g. vibrations, rotations or combinations of the two. They are associated to different distinctive range of energies, focusing on a general rotation we have energies, in broad terms, in the range $\Delta \varepsilon_{rot} \cong 10^{-4}$ eV, so from eq. 2.3:

$$T_{rot} \cong \frac{4 \text{ eV fs}}{10^{-4} \text{ eV}} = 4 \cdot 10^4 \text{ fs} = 40 \text{ ps} \qquad (2.4)$$

that is a quite short oscillation period. Considering instead the vibration degree of freedom we have $\Delta \varepsilon_{vibr} \cong 0.1$ eV, therefore:

$$T_{vibr} \cong \frac{4 \text{ eV fs}}{0.1 \text{ eV}} = 40 \text{ fs} \qquad (2.5)$$

that is an considerably shorter result. Regarding transitions between different electronic states $\Delta \varepsilon_{tr} \cong 1$ eV is a realistic possible approximation, giving us:

$$T_{tr} \cong \frac{4 \text{ eV fs}}{1 \text{ eV}} = 4 \text{ fs} \qquad (2.6)$$

It is now clear the importance of being able to generate pulses that can probe such fast dynamics. It is not possible to generate such pulses directly from commercially available lasers sources, indeed suppose to have a Ti:Sa, we can assume an output wavelength around 750 nm:

$$T = \frac{\lambda}{c} \cong \frac{750 \cdot 10^{-9} \text{ m s}}{3 \cdot 10^8 \text{ m}} = 2.5 \text{ fs} \tag{2.7}$$

so not enough for our purposes. To obtain something shorter we have to reduce the wavelength, e.g. a T=0.1 fs corresponds to about λ=30 nm, meaning a radiation in the XUV range. The process exploted to produce the pulses needed for this puropose is called high-order harmonic generation HHG.

2.1 High-Order Harmonic Generation

From an experimental point of view the process starts with focusing pulses of tens of fs, tens of mJ - μJ in a focal region reaching intensities of about $10^{13} - 10^{15}$W/cm^2. The focal region is filled with a gas , typically a noble gas (Argon was used in our case) 2.2. For a number of different non linear processes the odd harmonics of the fundamental radiation can be generated with an efficiency that follows a trend with a plateau and a cut-off law. Due to the symmetry of the physical system, it is not possible to produce even harmonics.
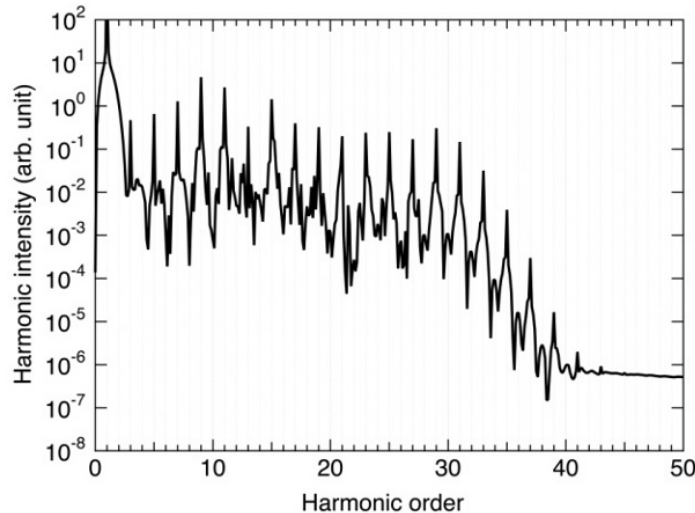
Figure 2.1: Typical trend of the efficiency of HHG [23]. In this case a plateau is present till the 30th harmonic and a cut-off right after.

The efficiency η is characterized by a plateau region with a typical value of $\eta \cong 10^{-5} - 10^{-6}$, requiring a huge number of photons to be exploited. A second observation is that, right after, is present a cut-off region that follows the equation:

$$\hbar \omega_c = I_p + 3.17 \, U_p \qquad (2.8)$$

where I_p is the ionization potential of the gas used and U_p is the ponderomotive energy ($U_p \propto I\lambda^2$, I intensity of the laser, λ its wavelength) that will be explained later.

Figure 2.2: Cell used in our experiments for the HHG through Argon.

2.1.1 Three step model (TSM)

This is a semiclassical model of HHG since the quantum mechanics is inherent in the ionization and recombination, but the propagation is treated classically [53].
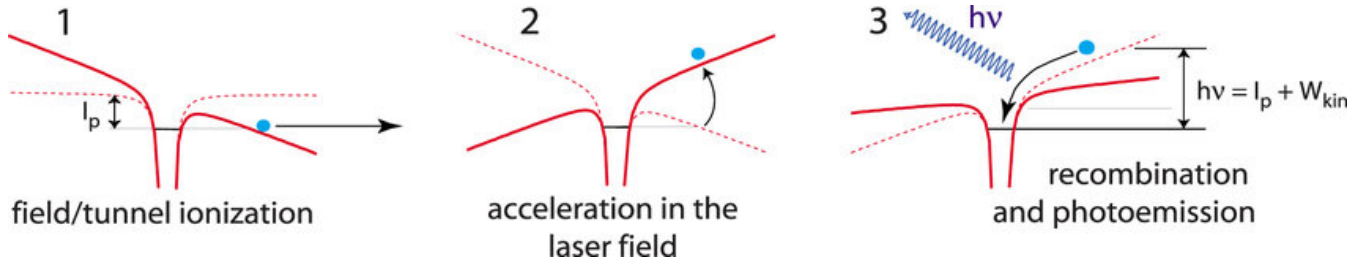
Figure 2.3: Illustration of the phases of the three step model for HHG [20].

In the TSM the potential of the system is described as the result of the interaction between the potential introduced by the laser and the one of the atom itself before the arrival of the radiation. This gives rise to a sloped shape with respect to the potential of the isolated atom as shown in 2.3.

According to this model we can split the process in three steps:

1. *tunnel ionization*: an electron is lifted to the continuum at the nuclear position with no kinetic energy in a tunneling ionization process through the potential barrier,

2. *propagation*: the subsequent motion of the electron is described classically as an acceleration in the laser electric field,

3. *recombination*: when the electron comes back to the nuclear position due to the deceleration caused by the electric field, occasionally, a radiation is emitted upon recombination. The corresponding photon energy photon is equal to the sum of the acquired electron kinetic energy and the ionization potential I_p.

We can write some equations to describe this model under the following assumptions: assume a classical model (II law of dynamics), the initial velocity of the electron is almost equal to zero, driving field is a continuous wave (CW) laser with the parent ion at $x = 0$ [1].

Let us consider a sinusoidal and linearly polarized field $E(t)$

$$\boldsymbol{E} = E_0 \, cos(\omega_0 t) \, \boldsymbol{u_x} \tag{2.9}$$

---

[1]Note that experimentally would not be possible to use CW lasers due to the high intensities that the process requires.

Classically the electron after the tunnelling can be described through:

$$m\frac{d\boldsymbol{v}}{dt} = -e\,E_0 cos(\omega_0 t)\,\boldsymbol{u_x} \tag{2.10}$$

where we can neglect the contribution of the coulomb potential due to the strong field approximation (SFA), we assume that E_0 is high in the initial moments, so we consider only the electric field term. So:

$$dv = -e\frac{E_0}{m}\,cos(\omega_0 t)\,dt \tag{2.11}$$

giving, after integration with initial velocity equal to zero:

$$v(t) = -\frac{eE_0}{m\omega_0}\,\left[sen(\omega_0 t) - sen(\omega_0 t')\right] \tag{2.12}$$

The position of the electron after the ionization, with $x_0 = 0$ at the parent ion, is:

$$x(t) = -\frac{eE_0}{m\omega_0}\,\left[cos(\omega_0 t) - cos(\omega_0 t') + \omega_0(t - t')\,sen(\omega_0 t')\right] \tag{2.13}$$

As said above the high harmonics are generated when the electron comes back to the parent ion, so if the eq. 2.13 has no solution for $x(t) = 0$ no HHG is possible. This motion equation is not solvable analytically, but studying its solution one gets that the generation of harmonics is possible if:

$$0 < \omega_0 t' < 80° \tag{2.14}$$

There are small temporal regions as the one in 2.14 repeating every $T/2$, so half the cycle of the fundamental radiation that allow the XUV generation. For higher values the electrons flies away and never returns to the paren ion, while for $t' = 0$ the electrons returns with a kinetic energy gain equal to zero, so no HHG is possible. The reason why XUV generated pulses are shorter than the optical period of the fundamental radiation is that the generation process is confined in a temporal window which is shorter than $T/2$.

According to the different value of the kinetic energy of the recombining electron the radiation emitted will have a different energy. To understand more precisely the phenomenon consider the following approximation for the solution of the eq. 2.13:

$$\omega_0 t = \frac{\pi}{2} - 3\cdot sin^{-1}\left(\frac{2}{\pi}\omega_0 t' - 1\right) \tag{2.15}$$

$$v(t) = -\frac{eE_0}{m\omega_0}\,\left[sin(\omega_0 t) - sin(\omega_0 t')\right] \tag{2.16}$$

17

so the energy of the photon emitted upon recombination is:

$$\hbar\omega_x = I_p + \frac{1}{2} m \frac{e^2 E_0^2}{m^2 \omega_0^2} \left[sin(\omega_0 t) - sin(\omega_0 t') \right]^2 \tag{2.17}$$

Assuming $t' = 0$ we get:

$$\varepsilon_k^{average} = \frac{e^2 E_0^2}{4 m \omega_0^2} = U_p \tag{2.18}$$

therefore the ponderomotive energy U_p corresponds to the mean kinetic energy of an electron which is oscillating freely in a sinusoidal field. We have:

$$\varepsilon_k = 2U_p \left[sin(\omega_0 t) - sin(\omega_0 t') \right]^2 \tag{2.19}$$

and combining this result with eq. 2.15 we get the following plot:
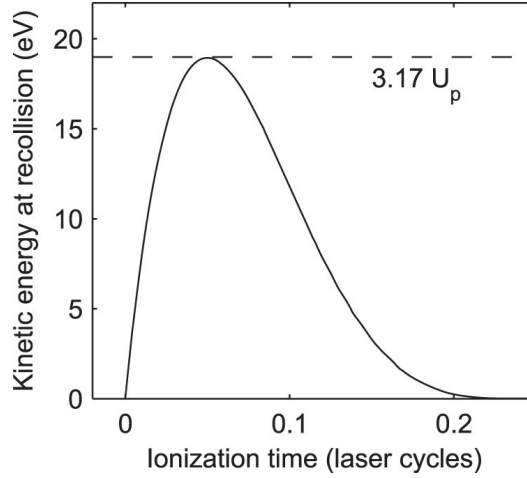
Figure 2.4: Kinetic energy of the electron at the time of recombination, as a function of the time of ionization [65].

From fig. 2.4 it becomes clear the maximum energy is obtained in correspondence of:

$$(\hbar\omega_x)_{max} = I_p + 3.17\, U_p \tag{2.20}$$

which is the cut-off law.

It is possible to obtain the same value of the kinetic energy of the recombining electron for two different values of t'. To understand this it is useful to plot the kinetic energy of the electron as a function of the time of recombination t instead of the time of the ionization t' as shown in fig.2.5.
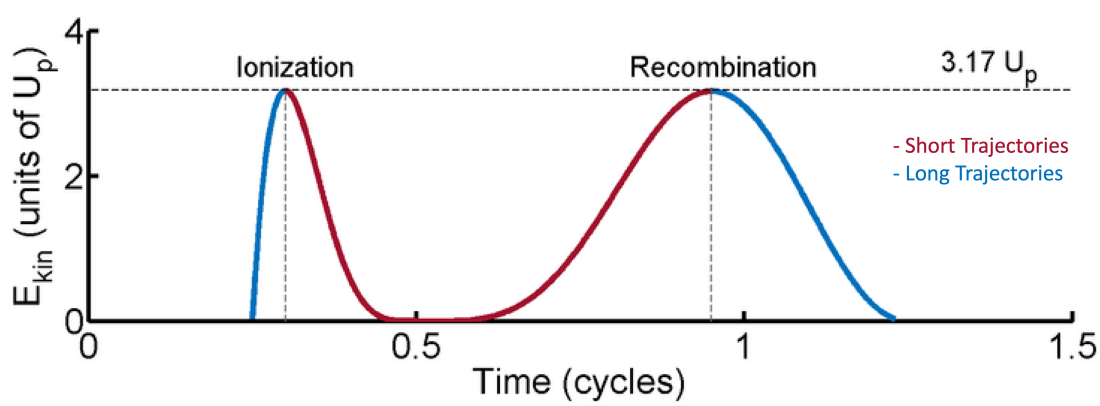
Figure 2.5: Kinetic energy of the electron as a function of the time of recombination [22]. Two different trajectories are possible: a long one and a short one.

In the figure there are two possible trajectories from the ionization bell to the the recombination: the short trajectories within the red section of the curve and the long trajectories within the blue section of the curve. They are not equivalent options. In the short case an increase of the time corresponds to higher values of the the electron kinetic energy ε_k, so an increase in the generated photon energy. For the long trajectories, to longer times correspond lower values of the electron kinetic energy ε_k, therefore a decrease in the generated photon energy. The consequence of this difference is in the chirp of the generated XUV pulses: short trajectories give rise to a positively chirped pulse, long trajectories to a negatively chirped pulse. Therefore the attosecond pulses generated by HHG are not transform limited, but there is a chirp at least for the components generated in the plateau region. This is of course not desirable, but it is possible to compensate it e.g. with metallic filter, like Al, that introduce negative dispersion to compensate the positive one of the pulses from short paths. These filters are typically used anyway due to the need of filtering out the IR radiation that is collinear with the generated, less intense, XUV radiation. Moreover, the XUV radiation generated by the short quantum path is highly collimated and it is not the same for the long path. This means that spatial characteristics of the former are usually better. So, is it possible to generate only short path pulses? Being able to do so represents an advantage also to obtain a single and coherent attosecond pulse, otherwise the synthesis of several harmonics coming from different paths with different phases often leads to an irregular attosecond pulse [25]. The answer is that there is a way and experimentally, the dominating trajectory is selected through phase matching by adjusting the position of the laser

focus relative to the nonlinear medium [18].

It is important to state that the TSM model is really helpful in a qualitative way to understand the phenomenon due to its simplicity with respect to other models. However it is not used as a basis to perform quantitative HHG simulations.

2.2 Quantum Description of the HHG

In this section a quantum description of the HHG process as seen in the previous section will be provided. Let's start from the equation for the electric field of the XUV radiation:

$$\frac{\partial^2 E_{XUV}}{\partial z^2} - \frac{1}{c^2}\frac{\partial^2 E_{XUV}}{\partial t^2} = \mu_0 \frac{\partial^2 P}{\partial t^2} \tag{2.21}$$

where the polarization vector is defined as:

$$\boldsymbol{P}(t) = n < e\boldsymbol{r}(t) >= n < \boldsymbol{r} > \tag{2.22}$$

where:

$$< \boldsymbol{r} >=< \psi(\boldsymbol{r},t)\,|\boldsymbol{r}|\,\psi(\boldsymbol{r},t) > \tag{2.23}$$

Consider an atom in strong laser field and in the single active electron approximation. We need to find the non linear polarization induced by the oscillating dipole. Consider for this purpose the Schrödinger equation:

$$i\hbar\frac{\partial\,|\psi\rangle}{\partial t} = H\,|\psi\rangle \tag{2.24}$$

where the hamiltonian can be written as:

$$H = H_0 + H' \tag{2.25}$$

H' takes into account the action of the electric field of the driving pulse on the system used for the XUV generation. H_0 is defined as:

$$H_0 = -\frac{\hbar^2}{2m}\nabla^2 + V(\boldsymbol{r} \tag{2.26}$$

V is the atomic potential, by considering the single electronic approximation we imagine one electron per atom interacts with the radiation. In atomic units $\hbar = m_e = e = a_0 = 1$ we have:

$$H_0 = -\frac{1}{2}\nabla^2 + V(\boldsymbol{r}) \tag{2.27}$$

and we will work within the electric dipole approximation framework, this is possible because the typical maximum separation of the electron from the parent ion is few nm, therefore much smaller than the driving radiation. With this approximation we can neglect the spatial dependance of $\boldsymbol{E}(t)$ and $\boldsymbol{A}(t)$ on the atomic dimension. We have:

$$H' = -\boldsymbol{\mu} \cdot \boldsymbol{E} = -e\boldsymbol{r} \cdot \boldsymbol{E}(t) = -\boldsymbol{r} \cdot \boldsymbol{E} \tag{2.28}$$

After the tunnel ionization we neglect the action of the Coulomb potential due to the SFA. The process is described as a transition from the ground state $|0\rangle$ to the continuum. The overall wavefunction is the coherent superposition of the $|0\rangle$ state and the continuous state:

$$\left|\psi_g\right\rangle = |0\rangle \, e^{-i\varepsilon_0 t/\hbar} = |0\rangle \, e^{iI_p t} \tag{2.29}$$

If the electron is free to move the kinetic momentum is:

$$\boldsymbol{p} = \hbar\boldsymbol{k} = \boldsymbol{k} \tag{2.30}$$

$$H_0 \left|\boldsymbol{k}\right\rangle = \frac{k^2}{2} \left|\boldsymbol{k}\right\rangle \tag{2.31}$$

In particular $|\boldsymbol{k}\rangle$ and $\left|\psi_g\right\rangle$ form a complete set, so we can write all $|\psi\rangle$ as a coherent superposition of them:

$$|\psi\rangle = e^{iI_p t} a(t) |0\rangle + \int dk^3 \, b(\boldsymbol{k},t) \left|\boldsymbol{k}\right\rangle \tag{2.32}$$

where $a(t)$ and $b(\boldsymbol{k},t)$ are amplitude functions. We can neglect the ground state depletion (even after tunnel ionization), so $a(t) \cong 1$. We have:

$$|\psi\rangle = e^{iI_p t} \left[|0\rangle + \int dk^3 \, b(\boldsymbol{k},t) \left|\boldsymbol{k}\right\rangle \right] \tag{2.33}$$

by defining a new amplitude b that takes into account the exponential term. We can now compute the expectation value of the dipole moment:

$$\langle\psi| = e^{iI_p t} \left[\langle 0| + \int dk^3 b(\boldsymbol{k},t) \langle\boldsymbol{k}| \right] \tag{2.34}$$

hence:

$$<\boldsymbol{r}> = \langle\psi|\boldsymbol{r}|\psi\rangle = \langle 0|\boldsymbol{r}|0\rangle + \int dk^3 \, b^*(\boldsymbol{k},t) \langle\boldsymbol{k}|\boldsymbol{r}|0\rangle + \int dk^3 \, b(\boldsymbol{k},t) \langle 0|\boldsymbol{r}|\boldsymbol{k}\rangle + \iint d^3k \, dk'^3 \, b^2(\boldsymbol{k},t) \langle\boldsymbol{k}|\boldsymbol{r}|\boldsymbol{k}'\rangle \tag{2.35}$$

It is possible to obtain a simpler expression. The first term $\langle 0|\,r\,|0\rangle$ is the matrix element of the dipole moment referred to the ground state, so it is a constant and we can neglect it since it does not oscillate. We can neglect also the fourth term since $\langle k|\,r\,|k'\rangle$ is the matrix element of the dipole moment associated to the transition from the continuous state k' to the continuous state k. We want to describe the transition from the continuous state to the ground state, so we are not interested in this possibility. The second element is the matrix element of the dipole moment corresponding to the transition from ground state up to the continuous state k. It is related to the ionization, but not to the oscillating dipole moment emitting the radiation. We can write:

$$\langle k|\,r\,|0\rangle = d(k) \tag{2.36}$$

$$\langle 0|\,r\,|k\rangle = \langle k|\,r\,|0\rangle^* = d^*(k) \tag{2.37}$$

Therefore one can write:

$$<r> = \int dk^3\, b(k,t) d^*(k) + c.c. \tag{2.38}$$

We don't know the function b, but we can find an expression for it. Changing variable of integration and moving from the kinetic momentum k to the canonical momentum we have:

$$m\frac{dv}{dt} = qE = -q\frac{dA}{dt} \tag{2.39}$$

$$\frac{d}{dt}(mv + qA) = 0 \tag{2.40}$$

$$p = mv + qA = mv - eA = v - A = k - A \tag{2.41}$$

We assume k does not change in the temporal interaction between tunnel ionization and recombination because we can neglect the action of Coulomb potential, so electron undergoes only the action of the field. So we can write

$$<r> = \int dp^3\, b(p,t)\, d^*(p + A(t))\, e^{-iS(p,t,t')} \tag{2.42}$$

where t' is the instant after the tunnel ionization and S the semiclassical action:

$$S(p,t,t') = \int_{t'}^{t} dt'' \left(\frac{(p+A(t))^2}{2} + I_p \right) \tag{2.43}$$

Eventually we end up with the equation:

$$<r(t)> = i\int_{0}^{t} dt' \int dp^3 d^*(p+A(t))\, e^{-iS(p,t,t')} E(t') \cdot d(p+A(t)) \tag{2.44}$$

22

In particular the first term $\boldsymbol{d}^*(\boldsymbol{p}+\boldsymbol{A}(t))$ represents the third step in the TSM, that is the recombination towards the ground state. The second term $e^{-iS(\boldsymbol{p},t,t')}$ is the second step in the TSM and represents the action accumulated by the electric field during its motion from tunnel ionization t to the recollision instant t'. Eventually the last term $\boldsymbol{E}(t')\cdot\boldsymbol{d}(\boldsymbol{p}+\boldsymbol{A}(t))$ describes the transition from ground state to continuous state at the instant t'. This ionization is induced by $\boldsymbol{E}$.

2.3   Multi Ionization Process: Keldysh Parameter

Consider the system in the fig. 2.6 and imagine an electron in the ground state E_g, how can this electron move to the continue through photons with an energy lower than the ionization potential, since there are no states with energies $E_g + \hbar\omega$, $E_g + 2\hbar\omega$ and so on?
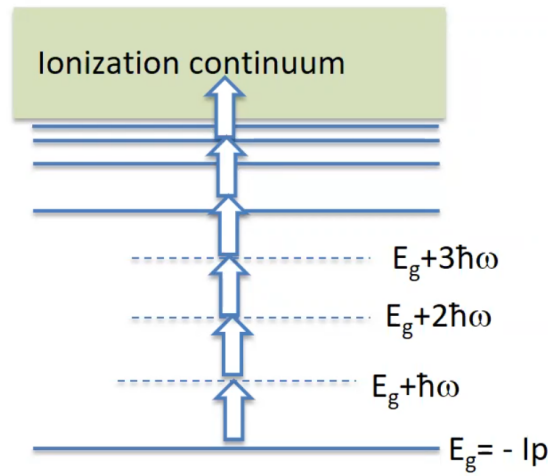
Figure 2.6: Multi ionization process.

As shown at the beginning of this chapter, through uncertainty principle we can provide an estimate of the time needed for the transition $\Delta t \sim \hbar/\Delta E$, as an example we can take $\Delta t \cong 50-100$ as. The electron does not know that there are no states with energies $E_g + \hbar\omega$ and multiples for a time Δt, therefore if enough photons are absorbed within this period the transition becomes possible. This means very intense light is needed. Indeed, considering typical pulse parameters as duration of 100 fs, energy of 1 µJ, wavelength of 1 µm, focused into 10 µm x 10 µm we obtain about $10^{14}-10^{15}$ W/cm^2.

In 1964 it was published the first paper which directly addresses this problem [27] by L. D.

Keldysh. In this work the famous Keldysh parameter γ is introduced and two different ionization regimes are identified.

The Keldysh parameter can be derived in a simplified picture of the system. Consider the system in the figure 2.7. The energy of the electron is given by three contributions: the kinetic energy ε_k, the Coulomb potential energy and the potential introduced by the laser.
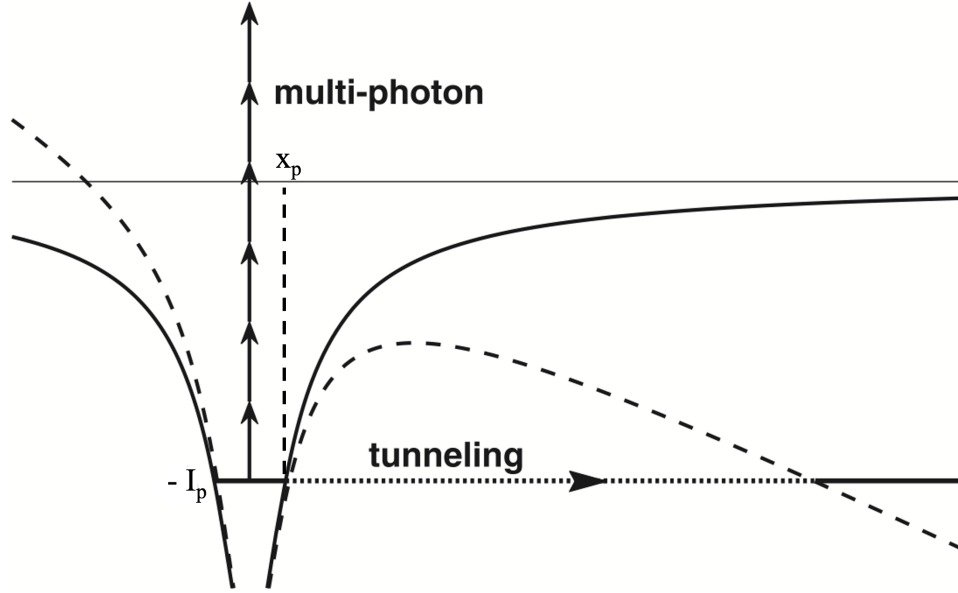
Figure 2.7: Schematic of multi-photon and tunnel ionization.

The driving radiation potential is given by $xE(t)$ and we can define the tunnel ionization time τ as:

$$\tau = \frac{x_b}{<v>} \tag{2.45}$$

where the thickness of the barrier x_b is defined as:

$$x_b = \frac{I_p}{eE_0} \tag{2.46}$$

The average velocity of the electron is assumed equal to:

$$<v> = \frac{v(0) + v(x_b)}{2} \tag{2.47}$$

For the SFA we have:

$$\frac{1}{2}mv^2(0) = I_p \tag{2.48}$$

24

Assuming $v(x_b) = 0$ and since $v(0) = \sqrt{2I_p/m}$ we have:

$$< v >= \frac{1}{2}\sqrt{\frac{2I_p}{m}} \tag{2.49}$$

so eventually:

$$\tau = \frac{2I_p}{eE_0}\sqrt{\frac{2I_p}{m}} = \sqrt{\frac{2I_pm}{e^2E_0^2}} \tag{2.50}$$

We can now introduce the Keldysh parameter γ:

$$\gamma = \omega\tau = 2\pi\frac{\tau}{T_0} = \sqrt{\frac{2\omega^2I_pm}{e^2E_0^2}} = \sqrt{\frac{I_p}{2U_p}} \tag{2.51}$$

This parameter allows us to identify two different regimes as showed in fig. 2.6:

- $\gamma << 1$ meaning $\tau << T$, so during the tunnel ionization process the electron sees the potential barrier as static,

- $\gamma >> 1$ meaning $\tau >> T$, so during the tunnel ionization process the electron sees the potential barrier rapidly oscillating and the process is possible via multi photon ionization.

It is important to understand that $\gamma >> 1$ does not really mean that the tunneling is not happening, but it means that the barrier is not static.

As shown in the section 2.1 the attosecond physics includes the ultrafast dynamics of electron tunneling, especially if we consider such an important process as the HHG. The Keldysh parameter gives a very important element to have a better understanding on processes that are at the fundamental of this science.

2.4 Characterization of Attosecond Pulses

In the years various different techniques have been developed to measure and characterize ultrashort pulses. A widely used and established technique for the reconstruction of pulses in the ps-fs range is the *Frequency-Resolved Optical Gating* FROG invented in 1991 by Rick Trebino and Daniel J. Kane [26]. Several alternatives exist: *Spectral Phase Interferometry for Direct Electric-field Reconstruction* SPIDER, variations on the FROG like SHG-FROG, PG-FROG, TG-FROG and son on. However if we move to the attosecond domain these options are not

exploitable anymore since they rely on optical domain, so optical tools. For XUV pulses other techniques are needed and this is due to the fact that the optical techniques have a non-linear nature. Indeed this makes them difficult to be applied to the XUV, typically characterized by the absence of sufficient non-linearity. The most widely used techniques for the study photoemission dynamics are the *Reconstruction of Attosecond Beating By Interference of Two-photon Transitions* RABBITT [43] and attosecond streaking spectroscopy [24].

2.4.1 Attosecond Streaking Camera

In principal the functioning of an attosecond streaking camera ASC is similar to a conventional streaking-camera fig.2.8, however the latter can perform measurements at best up to the ps range. In the conventional case a change of the amplitude of a voltage in time is used to accelerate photoelectrons to different velocities according to the value of the voltage the are subject to. So photoelectrons coming in different instants, therefore different delays of the incident pulse, are coupled to different spatial positions due to the different acceleration they underwent.
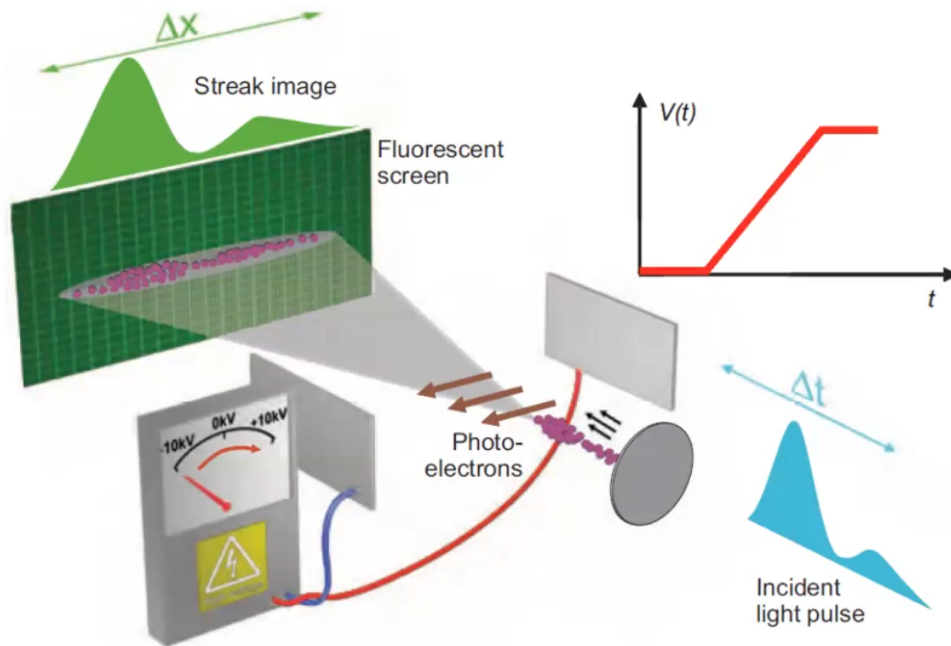
Figure 2.8: Schematic a conventional streaking camera.

In the ASC case a faster change in the voltage than the ps range is needed, so an ultrafast

pulse can be exploited and in particular its field gradient.

The principle is mapping the pulse we want to measure in the photoelectron wave function. This can be done by photoionizing an electron with the attosecond XUV pulse we want to measure, the electron wavefunction will encode the information about the pulse that was used. Subsequently the electron is probed by an IR pulse 2.9.
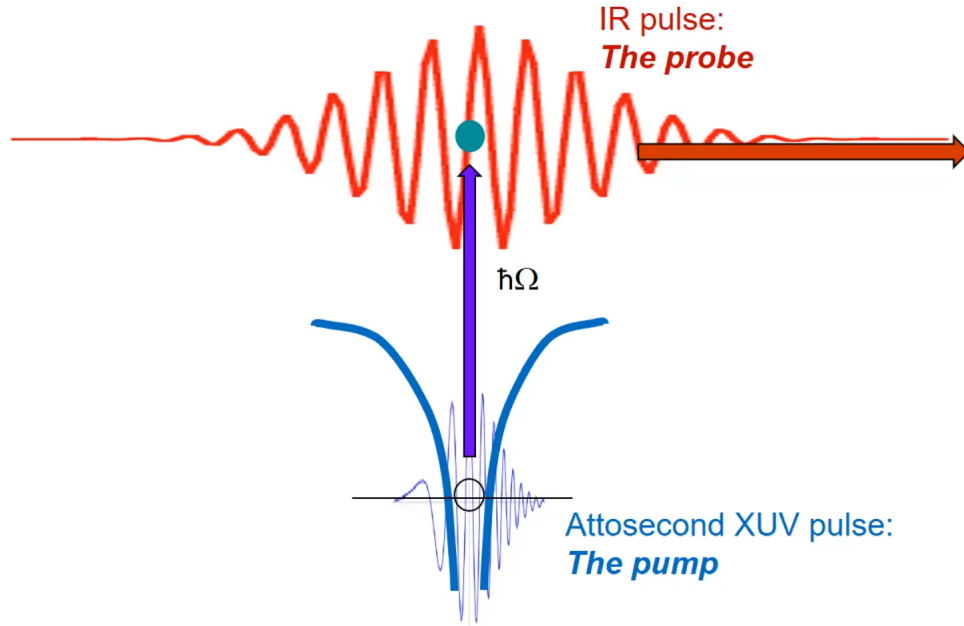
Figure 2.9: Attosecond Streaking Camera working principle.

The velocity of the electron will depend on the moment it is realised, since different frequency values of the XUV pulse will correspond to different kinetic energies of the electron. This creates a velocity shift just like in a conventional streaking camera. Its momentum can be written by conservation law as:

$$\frac{p_0^2}{2} = \hbar\Omega - I_p \tag{2.52}$$

where Ω is the frequency of the attosecond pulse. The electron will the interact with the oscillating IR pulse that will change its momentum, giving a final momentum of the electron on the detector equal to:

$$\boldsymbol{p}_f = \boldsymbol{p}_0 - \boldsymbol{A}_{IR}(t_{ion}) \tag{2.53}$$

so p_f depends on the initial momentum and the IR pulse potential vector evaluated at the time of the ionization. Since the vector potential changes on a fast time scale we map the time of the

ionization on the final momentum. Suppose now to change the delay between the IR and the XUV pulses as shown in fig.2.10.
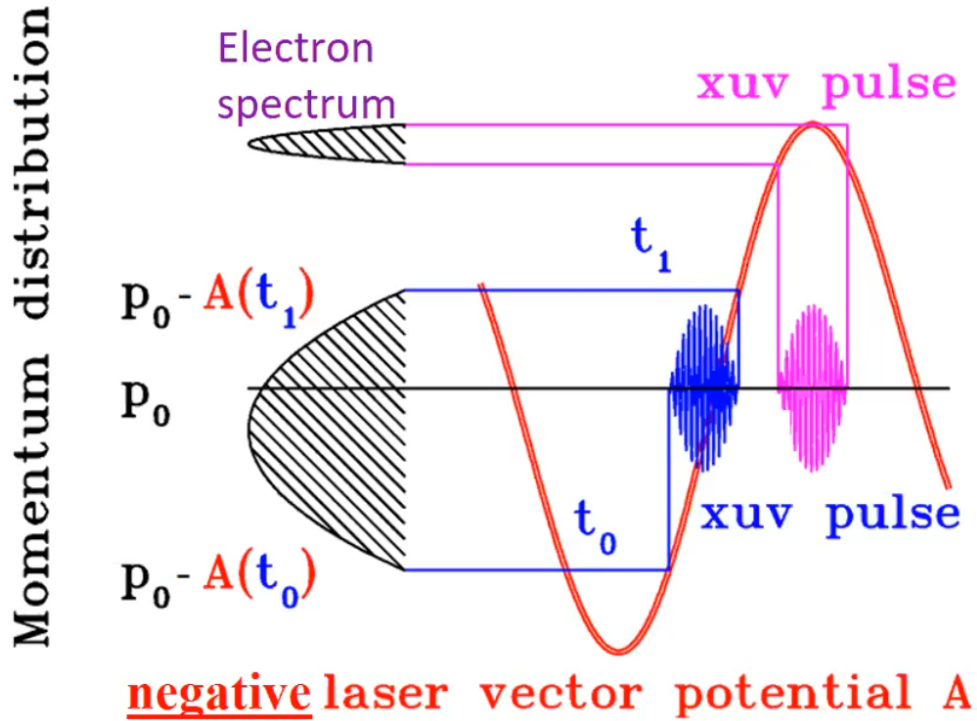
Figure 2.10: Effect on the momentum distribution of the different delays between the attosecond and IR pulses.

Consider two different attosecond pulses, one (blue pulse in fig.2.10) arrives at the zero of the oscillating vector potential of the IR field and the other (pink pulse in fig.2.10) on the maximum. We are interested in the photoelectron momentum spectrum on the detector. It is clear from the scheme in fig.2.10 that the blue pulse (minimum of A_{IR}) will generate a wider momentum distribution with respect to the narrow spectrum of the pink one (maximum of A_{IR}). This distinction is possible as long as the XUV pulse is shorter than a quarter of the period of the IR pulse.

This technique allows also for a measurement of the chirp of the XUV pulse. Indeed, this information is recorded by the process, consider the momentum of the electron after the ionization in eq.2.52, it depends on the instantaneous frequency of the XUV pulse $\Omega(t)$, therefore the chirp in the spectrum of the pulse will be mapped in the momentum of the electron. In particular if the XUV pulse delay is such that the electron meets the IR pulse when $-A_{IR}$ is increasing then $p_0(t)$

goes up if $\Omega(t)$ increases and thus the spread of the momentum is going to be larger compared to the case without any chirp. If the delay is such that the electron meets the IR pulse when $-A_{IR}$ is decreasing then $p_0(t)$ goes up if $\Omega(t)$ decreases, so the spread of the momentum will be lower with respect to the previous case. This generate an asymmetry in the oscillation of the spectrum as shown in fig.2.11.
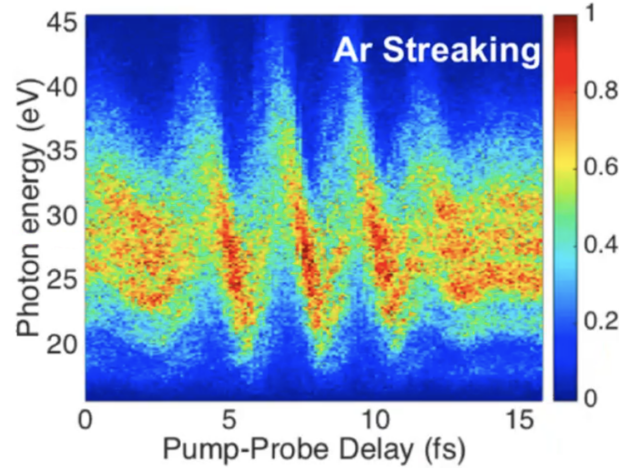
Figure 2.11: Effect on the spectrum of XUV pulse chirp [9].

From a mathematical point of view the transition amplitude to the final state in the continuum $|p_f\rangle$ of the extracted electron with momentum p, can be described, in the SFA (considering the final state to be a plane wave), by the formula (atomic units are employed):

$$a(\boldsymbol{p}, \tau) = -i \int_{-\infty}^{+\infty} e^{i\phi t}\, \boldsymbol{d}_{p(t)} \cdot \boldsymbol{E}_X(t - \tau)\, e^{i(W + I_p)t}\, dt \tag{2.54}$$

$$\phi(t) = -\int_{t}^{+\infty} \left[\boldsymbol{p} \cdot \boldsymbol{A}(t') + \frac{\boldsymbol{A}^2(t')}{2} \right] dt' \tag{2.55}$$

where $\boldsymbol{p}_f(t) = \boldsymbol{p}_0 + \boldsymbol{A}(t)$ is the instantaneous momentum of the free electron in the laser field, $\boldsymbol{d}_p$ is the transition dipole matrix element from the initial state to the final continuum of states and $W = \boldsymbol{p}^2/2$ is the electron final kinetic energy. The scalar product $\boldsymbol{d}_p \cdot \boldsymbol{E}_X$ represents the electron wavepacket generated in the continuum by the XUV field, on which it is induced a temporal phase modulation $\phi(t)$ by the dressing IR field.

2.4.2 RABBITT

The Reconstruction of Attosecond Beating By Interference of Two-photon Transitions is another technique employed for the reconstruction of attosecond pulses, in particular for train of attosecond pulses ATP [43]. The RABBITT technique consists in the acquisition of photoemitted electron spectra from a noble gas as a function of the delay between the APT, which ionizes the gas, and a dressing IR pulse. Since in the HHG scheme only odd harmonics are generated, the energy of the photoemitted electrons is an odd multiple of the IR energy minus the ionization potential of the target gas:

$$\varepsilon_q = (2N+1)\hbar\omega_{IR} - I_p \tag{2.56}$$

where N is an integer number identifying the order of the harmonic. After the photoemission caused by the XUV, electrons can interact with one or more IR photons that induce additional transitions in the continuum. In particular, if we only consider interactions with a single IR photon, it can be either absorbed or emitted.
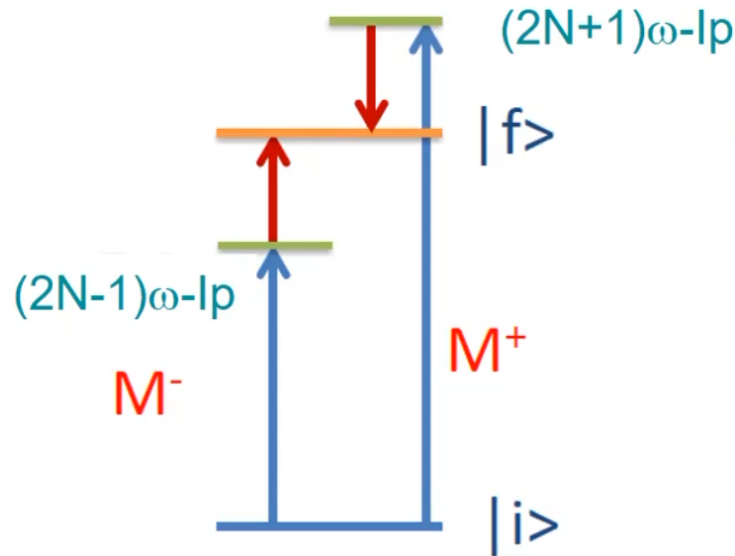
Figure 2.12: RABBITT physical principle.

Like shown in fig.2.12 two possible paths can give rise to an electron with the same energy. Indeed, considering two consecutive harmonics $2N+1$ and $2N-1$, it is possible to have the emission of a IR photon prom the electron ionized by the $2N+1$ harmonic and the absorption of an IR photon by the electron ionized by the $2N-1$ harmonic. These two different paths create

an interference, the so called sideband like shown in fig. 2.13 where the interference periodic patterns are visible between the bends due to the harmonics ionizations.
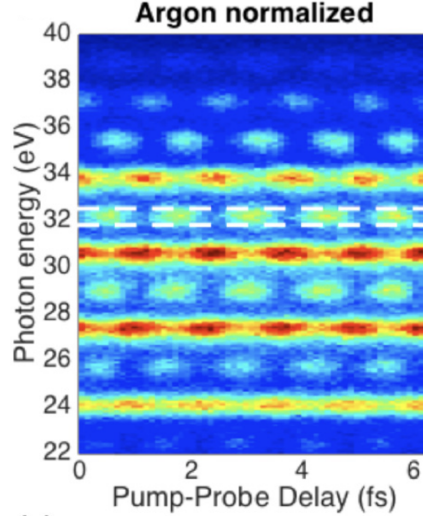
Figure 2.13: RABBITT traces for Ar 3p measured with an XUV-APT pump and an IR probe [9]. One sideband pattern is highlighted between the white dotted lines.

In case of low IR field intensity, we can describe this using a second order perturbation theory, so each harmonic has only one sideband per side. As a result, the sideband oscillates as the delay τ between the IR and XUV pulses is scanned. In particular applying Fermi's golden rule in the second order perturbation framework and assuming monochromatic IR field and XUV harmonics, the $2N$ sideband signal can be written as:

$$SB_{2N} \propto cos(2\omega_{IR}t - \Delta\phi_{XUV} - \Delta\phi_{at}) \tag{2.57}$$

where t is the delay between the pump and the probe pulse, $\Delta\phi_{XUV}$ represents the additional phase term acquired due to the chirp of the APT and $\Delta\phi_{at}$ refers to the atomic scattering phase, which in terms of time delays becomes to:

$$\tau_{at} = \hbar\frac{\partial\phi_{at}}{\partial\varepsilon} \cong \hbar\frac{\Delta\phi_{at}}{\Delta\varepsilon} \tag{2.58}$$

This time delay in the RABBITT techniques consists of a sum of two terms: the Wigner time delay τ_W and the continuum-continuum time delay τ_{CC} [30]. With τ_W it is measured the group delay experienced by electron wave packet under the short-range influence of a Coulomb potential with respect to a free electron with the same kinetic energy. The additional term τ_{CC}, on

the other hand, is measurement-induced and is introduced in the additional quantum transition between two electronic states in the continuum with the IR probe pulse interaction. With this technique, one can thus extract information on the XUV attosecond pulse train chirp, mainly considering $\Delta\phi_{XUV}$ (given that $\Delta\phi_{at}$ is much smaller) or about the time delay in photoemission, focusing on $\Delta\phi_{at}$ (since $\Delta\phi_{XUV}$ is independent from the target).

In the specific case of the present work, we deal with a single harmonic. Therefore the photo-electron trace we worked with is characterized by the presence of a main band due to the pho-toelectrons that were emitted by the XUV pulse and two sidebands created by the subsequent interaction of the photoelectron with the UV signal. An example of this kind of photoelectron trace is reported in fig.2.14.
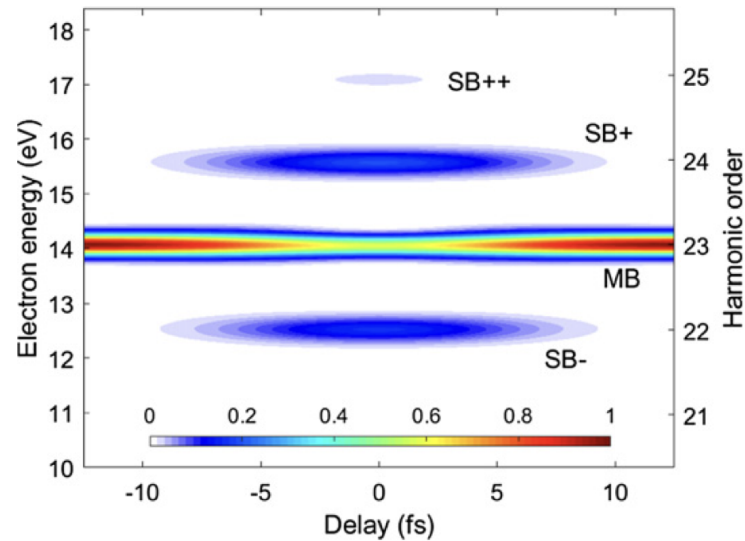
Figure 2.14: Example of a single harmonic spectrogram [41].

The reconstruction of the experimental photoelectron traces of this kind is at the core of the pulses temporal characterization.

3. Experimental Setup

In fig.3.1 is represented a simplified scheme of the whole experimental setup exploited for all the analysis and experiments described.
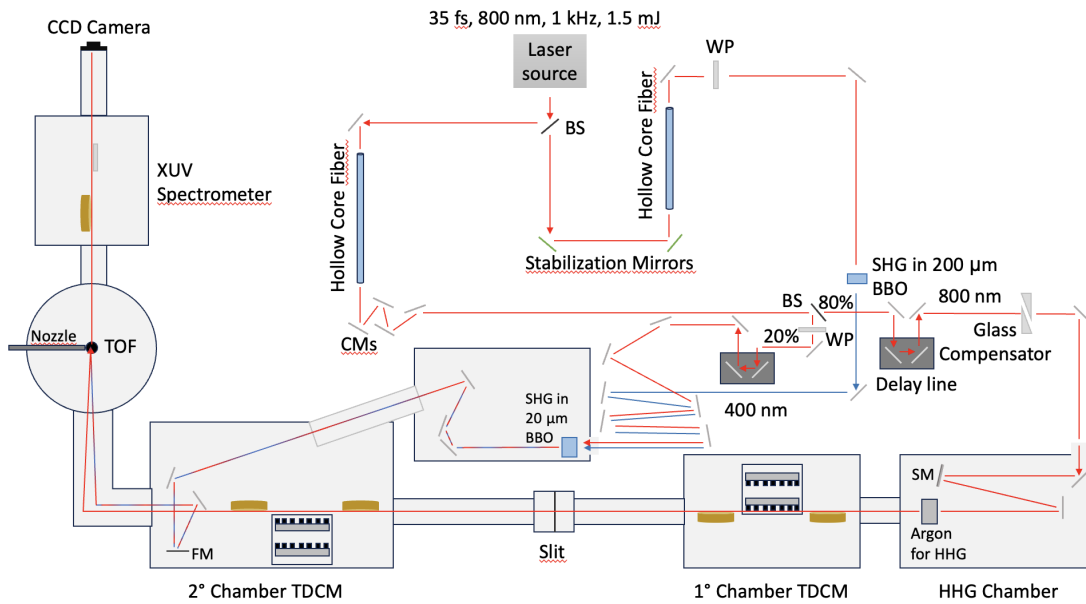
Figure 3.1: Simplified scheme of the complete experimental setup.

The main laser source is a Coherent Astrella Ti:Sa producing 35 fs at 800 nm with 1 kHz repetition rate and an energy of 7 mJ of which 1.5 mJ are exploited. The output is divided into two different beam lines through a beam splitter with a ratio 80% (reflection)- 20% (transmission). The 80% reflection branch is further split in two 50% branches of which just one branch is used for these experiments. In the following the two lines are analysed separately.

The 80% beam line is employed for the ultimate goal of the pump UV generation. The beam is led, after some bounces through mirrors and a pair of stabilization mirrors, into a hollow core fiber to obtain a better spacial shape on the output. A wave plate is employed to regulate the intensity and eventually the beam is used to perform a SHG (*second harmonic generation*) through a 200 μm BBO crystal. The output are narrow-band pulses at 400 nm that will be superimposed with visible/IR pulses to create the UV signal.

The 20% beam line purpose is to produce the probe XUV through the HHG and to provide the line for the production of the pump UV. The beam is propagated into a hollow core fiber to perform a compression and obtain shorter pulses through a spectral broadening, therefore obtaining a 5 fs at 600 - 1100 nm at the output. After the fiber, chirped mirrors (CM) are placed to compensate for the dispersion introduced previously. After that, the beam meets a second beam splitter with a ratio 20% - 80%.

The 70% branch goes through a delay stage controlled both manually and with a piezoelectric actuator for fine adjustments and a glass medium to compensate for the dispersion, eventually it enters in the chamber dedicated to HHG in argon. Various harmonics are produced from the 800 nm used for the generation with the efficiency depending on different elements of the setup: gas pressure, output mode from the fiber, thickness employed in the glass compensator and so on. Once the harmonics are generated the one intended to be epmloyed in the experiment has to be selected and this is done through two TDCM (*time-delay compensated monochromator*) [48], usually being the 25th, so at 38.75 eV. The efficiency of the TDCM is around 20-30%.

The 30% is used for the generation of the UV pulse. After the beam splitter a wave plate is used to regulate the intensity of the beam and a time delay to allow the superposition between the 800 nm and the 400 nm coming from the other line of the first beam splitter. The beam, along with the 400 nm, is bounced on some mirrors and enters the SHG chamber. Once the two mentioned beams are spatially and temporally superimposed they can generate the UV pump pulses centered at 270 nm with μJ-level energy. This generation is done by frequency up conversion between the sub-10 fs visible/IR pulses and the narrow-band pulses at 400 nm in a 20 μm Type-I BBO crystal. This process is characterized by an efficiency around the 10%. The UV line is then led back to the XUV line and together are exploited to carry out the experiments in the chamber with the samples to be analysed. The final pulses were reconstructed finding a duration of about 5 fs and 15 fs respectively for the XUV and UV.

Spatially overlapped probe and pump pulses propagate into the next chamber where the sample lies. Here a TOF (*time of flight*) spectrometer is placed to perform the measurements on the photoelectron emitted by the sample as a function of the UV-XUV delay. TOF spectrometers are composed by a stack of plates (which accelerate the particles), a flying tube and a detector

(typically a microchannel plate (MCP)-coupled to a scintillator and a photomultiplier tube). The last element consists in a XUV photon spectrometer ending in a CCD camera.

Hollow Fiber Compression

Hollow-core fiber compression of femtosecond light pulses is a well established compression technique to generate extremely short laser pulses. The fiber, unlike the more conventional types, is characterized by a hollow core that can be filled with a gas like in the case of this setup. Spectral broadening induced by SPM (*self-phase-modulation*) in gas-filled hollow fibers can lead to the generation of high-energy supercontinua, covering more than two octaves, thus offering the possibility to generate pulses with a transform-limited duration below 2 fs [68]. In the case of the present setup we report in fig.3.2 the result of an experimental frequency-resolved optical gating FROG performed at the output of the hollow fiber.
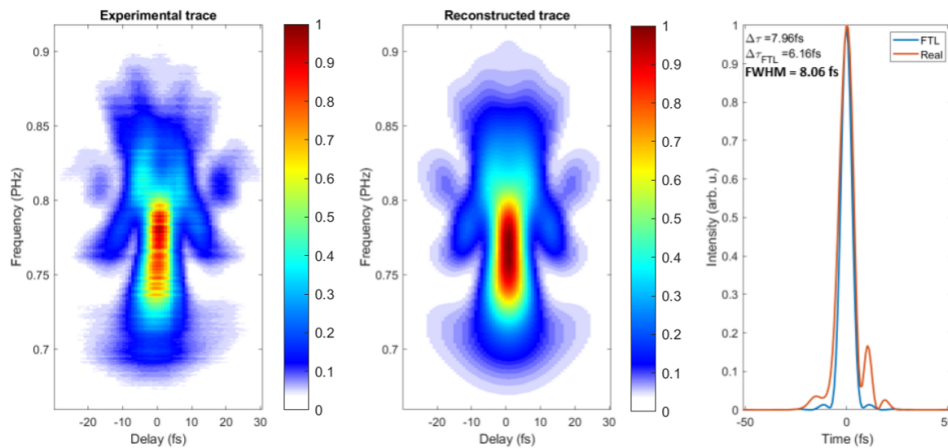
Figure 3.2: Experimental FROG showing the performance of the post-compression.

As it appears from the image the FWHM of the output pulses is around 8 fs.

TDCM

The optical design of the TDCM is shown in fig.3.3.
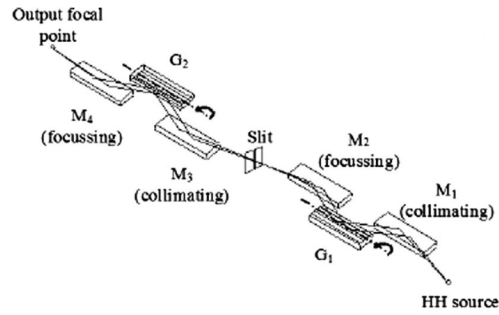
Figure 3.3: Optical design of the TDCM.

The whole TDCM setup is accurately described in [48]. Each of the two TDCM chambers is composed by two toroidal mirrors, a collimating and a focussing one, and a plane grating. The first section is a conventional monochromator giving a spectrally dispersed image of the source on the intermediate plane. The slit lies exactly on this plane allowing to carry out the spectral selection of the HHs. This means that only a selected portion of the spectrum, that is one single harmonic during the experiments, is allowed to propagate through the slit toward the second section. This section is specular with respect to the first one to realize the compensation and to give a monochromatic and stigmatic output focus. Both gratings are plane and operated in parallel light so each of the two sections has a collimating entrance mirror and a focusing exit mirror.

4. XUV and UV Pulse Reconstruction

In this chapter the first part of the work will be explored. It concerns the reconstructions of the UV pump and the XUV probe pulses that were employed in the experiments of ultrafast spectroscopy on molecules.

4.1 Methodology

As shown in section 2.4 there are various different methods to characterize and reconstruct pulses in the XUV range that are not equivalent to each other, the attosecond streaking is employed for IAPs, while the RABBITT technique is exploited for ATPs reconstruction.
In the present case we deal with pulses for pump and probe spectroscopy requiring a precise harmonic of the fundamental at 800 nm to be used, therefore there is no interest in reconstructing the relative phase between the different harmonics generated, since they are stopped upstream. Therefore there is no need to employ algorithms based on techniques like RABBITT if some faster and well performing options are available. For these reasons an approach called Simplified Trace Reconstruction In the Perturbative regimE STRIPE was adopted [40], as a matter of fact this method is not based on a phase retrieval algorithm, therefore it is typically much faster than the other ones currently known.

4.1.1 The STRIPE model

Here a brief explanation of the model used is presented. In the SFA, the photoionization process of a rare gas, in the presence of XUV and UV pulses can be described by the following formula (atomic units are used):

$$S(\boldsymbol{p},\tau) = \left| \int_{+\infty}^{-\infty} dt\, E_{XUV}(t+\tau)\, e^{i\phi(\boldsymbol{p},t)} e^{i\left(\frac{p^2}{2}+I_p\right)t} \right|^2 \tag{4.1}$$

where $E_{XUV}(t)$ is the XUV pulse, $\phi(\boldsymbol{p},t)$ is a phase term which accounts for the effect of the UV field on the phtoelectron wavepacket of momentum p, I_p is the atomic ionization potential and τ is the relative delay between the XUV and UV. This model can be further simplified by

applying some approximation, indeed under the the central momentum approximation (CMA), the perturbative approximation and the slowly varying envelope approximation (SVEA), we can write:

$$S(\omega, \tau) \cong \left| \int_{+\infty}^{-\infty} dt \, E_{XUV}(t+\tau) \, e^{i\frac{p_c}{\omega_0^2}E_{UV}(t)} \, e^{i\omega t} \right|^2 \qquad (4.2)$$

where we set $\omega = \frac{p^2}{2} + I_p$. The eq.4.2 represents the model upon which STRIPE is based. Summing up the advantages of the present method, it allows to reconstruct the pulses in a much faster way and with high degree of ac- curacy, despite all the approximation introduced and it is intrinsically robust against any level of noise.

The algorithm based on STRIPE was implemented in MATLAB.

4.2   Data

Like any other reconstruction method, STRIPE requires precise data in input which will greatly influence the results obtained by the algorithm.

First of all both the XUV and UV pulses spectra are required. The former is a spectrum of the 25-th harmonic generated form the fundamental at 800 nm, while the latter is centered around 270 nm as explained in the chapter 3. They are both showed in fig.4.1.

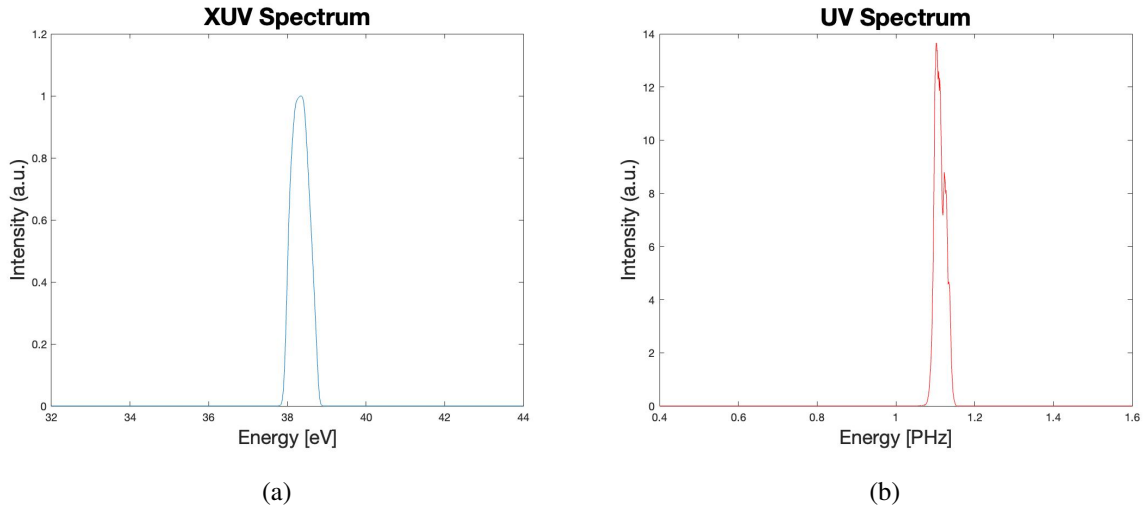(a)   (b)

Figure 4.1: (a) XUV spectrum in eV axis, (b) UV spectrum in PHz (petahertz) axis

The XUV spectrum obtained from the photoelectron spectrum in fig.4.2 will be used instead

of the one in fig.4.1a as explained after.

Photoelectrons XUV Spectrum
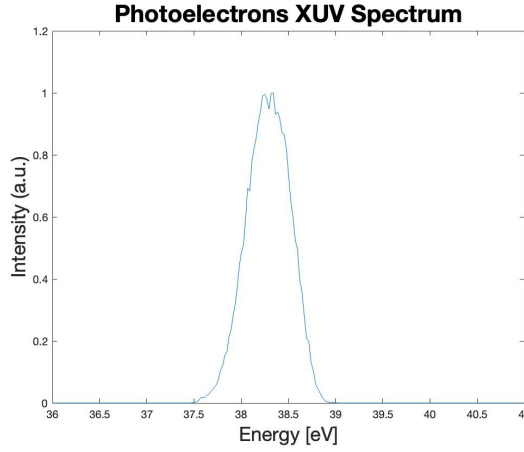
Figure 4.2: XUV spectrum in eV axis obtained from photoelectron trace.

STRIPE needs also the XUV-UV photoelectron trace (PON-pump on) and the XUV only photoelectron trace (POF-pump off). The traces are characterized by the delay between the pump UV and probe XUV on one axis and the TOF (time of flight) converted in kinetic energy in eV of the phototelectron on the other one. They are both traces where to each couple delay-energy corresponds an intensity value of the photoelectron collected by the TOF spectrometer coming from Argon atoms with a ionization potential $I_p = 13.99961$. The PON will contain the interference represented by the sidebands and therefore what is exploited to reconstruct the pulses, while POF is taken as background. Both are showed in fig.4.3.

The TOF spectrometer does not return directly the right energy axis, but it needs to be calibrated. For this reason a reference spectrum where some known harmonics of the fundamental are present is necessary. Knowing what harmonics appear in the reference spectrum allows to set the right value of energy for them. Subsequently the measurements taken have to be calibrated with that reference spectrum. To pass from the TOF axis to the kinetic energy the following function is employed for the fit:

$$f_{tof->E_k}(x) = c_1 x^{c_2} \qquad (4.3)$$

This procedure allows to obtain the energy axis which, along with the delay and frequency (in PHz) axis, is another parameter to be passed to the STRIPE algorithm in input.
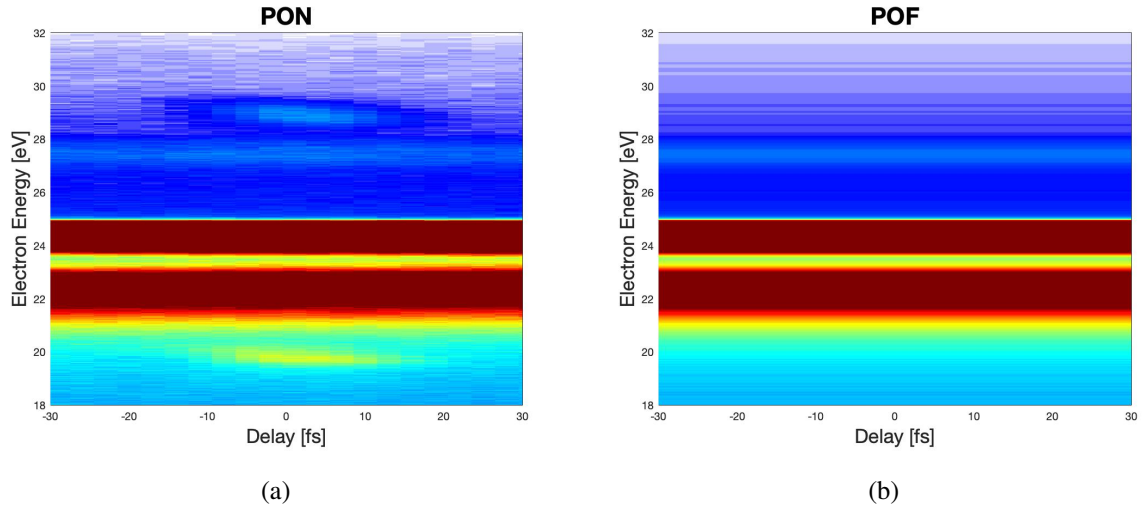
Figure 4.3: (a) XUV and UV photoelectron trace PON. Both the sidebands are visible, one at one UV photon energy above the main band (absorption by the photoelectron), the other at one UV photon energy below the main band (emission by the photoelectron), (b) XUV only photoelectron trace POF.

An analog calibration procedure has to be performed for the the XUV spectra to move from the pixel axis to the energy one. The first step is to move from the pixel axis to the wavelength through a fit made with the following function:

$$f_{px->wv}(x) = c_1 x^2 + c_2 x + c_3 \tag{4.4}$$

Finally the conversion from wavelength to energies is made with the simple relation:

$$\varepsilon_k = \frac{ch}{\lambda e} \tag{4.5}$$

where e is the unit of charge.

4.3   Results

The implemented MATLAB algorithm of STRIPE does not take in input only the data shown in the previous section 4.2, but initial guesses on some parameters are necessary. These parameters are:

- central wavelength of the UV spectrum in *nm*,

- bandwidth of the UV pulse,

- UV constant phase term,

- UV pulse group delay dispersion GDD in fs^2,

- UV pulse third order dispersion TOD in fs^3,

- UV pulse fourth order dispersion in fs^4,

- UV pulse intensity in TW/cm^2,

- amplitude of the XUV spectrum,

- XUV constant phase term,

- XUV pulse first order phase component fs^1,

- XUV pulse group delay dispersion GDD fs^2,

- XUV pulse third order dispersion TOD fs^3,

- a general amplitude term.

For all these parameters a range of values around the initial guess is also defined.

The final goal is to reconstruct the XUV and UV pulses on the temporal domain. To do so it is necessary to reconstruct as best as possible the experimental trace of photoelectron containing the interference signal as sidebands. The input data and the initial values of the parameters listed above are used to compute an initial guess for the photoelectron trace. Subsequently the STRIPE algorithm performs a defined number of iterations to minimize the sum of squares of the residuals of the difference between the computed and the experimental traces. This is done by the means of the MATLAB function *lsqnonlin*. In particular it solves nonlinear least-squares curve fitting problems of the form:

$$\min_{x} \|f(x)\|_2^2 = \min_{x} \left(f_1(x)^2 + f_2(x)^2 + \ldots + f_n(x)^2 \right) \tag{4.6}$$

The *lsqnonlin* parameters were set as reported in the appendix.

4.3.1 Issues with input data

The nature of the algorithm requires to test many different combinations of the starting parameters values to find the best reconstruction possible. In the following, some significant tries will be showed to highlights the problems rose with the data and the how they were solved.

In fig.4.4 one of the first attempts of reconstruction is reported considering the positive sideband.

(a)   (b)
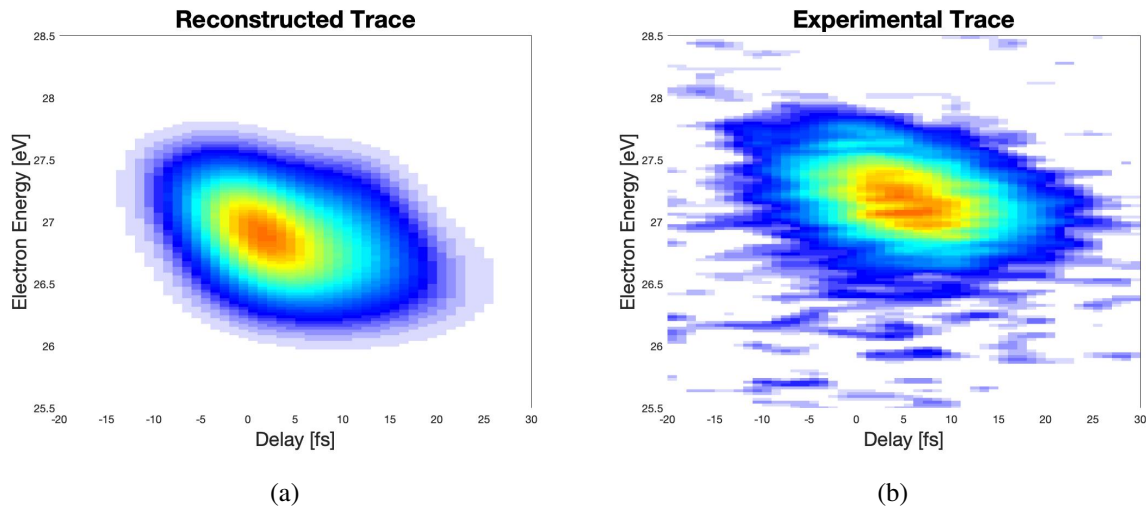
Figure 4.4: (a) Reconstructed positive sideband with STRIPE algorithm. The decentering along the energy axis is evident, (b) Experimental reference positive sideband.

Regardless of the quality of the computed sideband, an important issue has to be highlighted: the decentering of about 0.5 eV on the energy axis towards lower values with respect to the experimental reference. Since the shift is present on both sidebands, both towards lower values, it can not be related to a shift in the spectrum of the UV. However a shift in the XUV spectrum could give rise to the same decentering in both sidebands. This was verified by manually shifting the spectrum of the XUV signal trying to obtain the best match. One of the results is showed in fig.4.5.
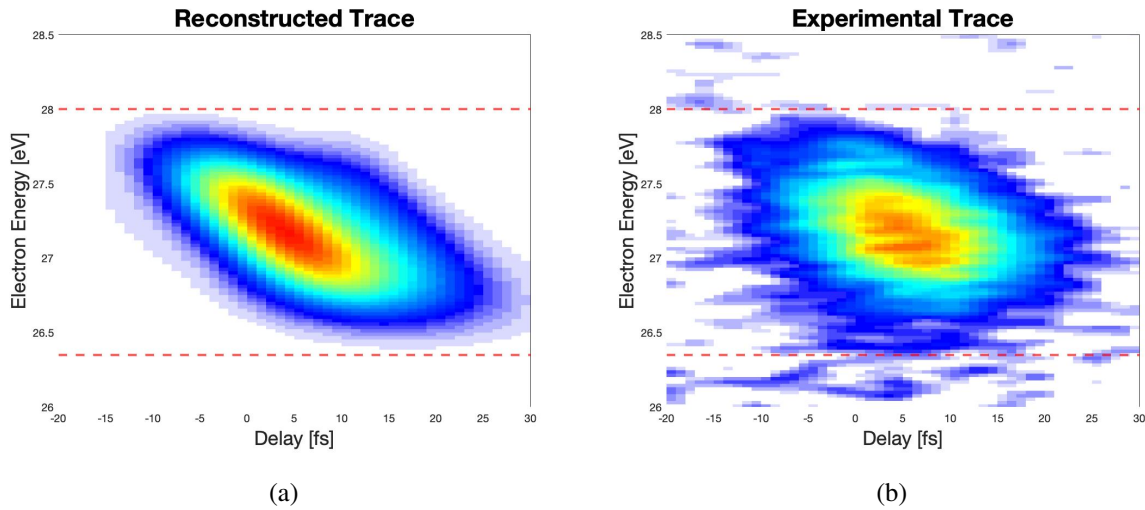
Figure 4.5: (a) Reconstructed positive sideband with STRIPE algorithm, (b) Experimental reference positive sideband.

The centering is better, the proof comes from the computed integral along the delay axis obtaining the spectrum of the sideband as shown in fig.4.6.
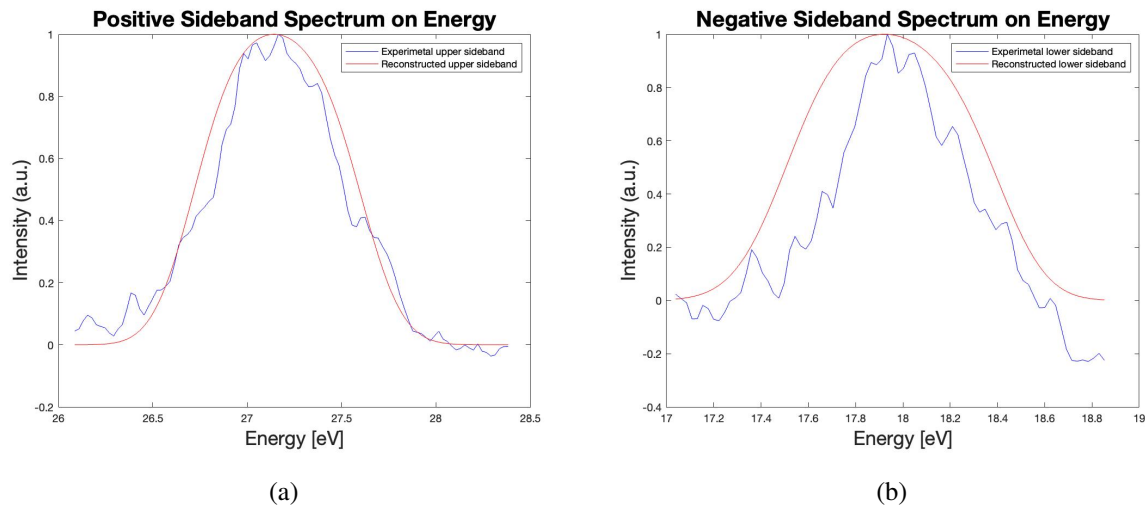
Figure 4.6: (a) Spectrum of the positive sideband resulting from the integration along the delay axis. Both the experimental and reconstructed spectra are showed, (b) Spectrum of the negative sideband resulting from the integration along the delay axis. Both the experimental and reconstructed spectra are showed.

The decentering however was not the only problem in the XUV spectrum. Indeed the computed negative sideband always presented a tilt too big compared to the reference one, an example is reported in fig.4.7.

Figure 4.7: (a) Reconstructed negative sideband with STRIPE algorithm. The very bad tilt and stretch is well visible in this example, (b) Experimental reference negative sideband.

The figure highlights the very bad tilt and stretch of the negative sideband, even without a problem in the centering as shown in fig.4.8.
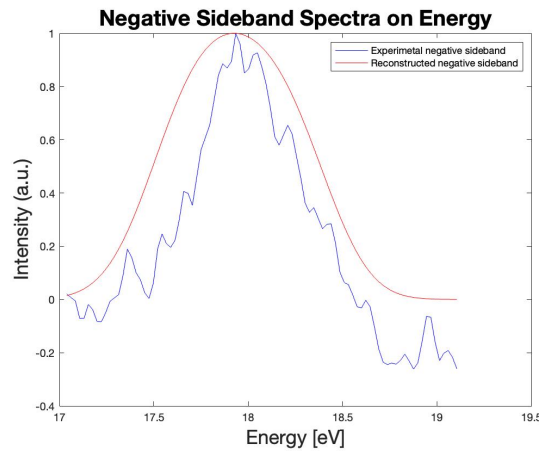
Figure 4.8: Spectrum of the negative sideband resulting from the integration along the delay axis.

This issue could be attributed to a XUV spectrum with a too wide *full width at half maximum*

FWHM. To verify this hypothesis the XUV normalized spectrum was elevated to different powers to decrease the FWHM and check the effects on the reconstructed sidebands. The resulting negative sideband, after providing in input to STRIPE a spectrum elevated to the fourth power, is showed in fig.4.9.

(a)

(b)
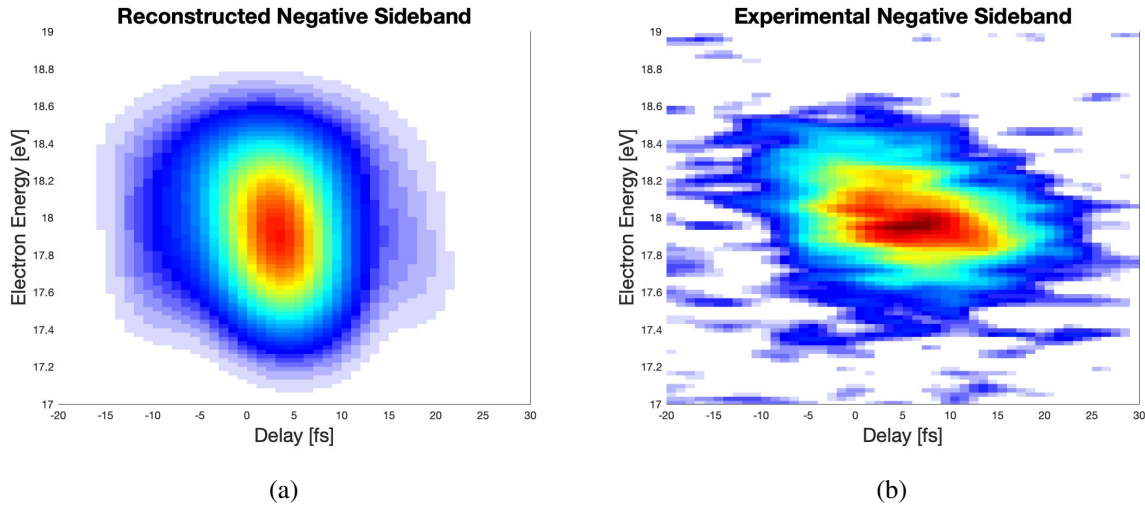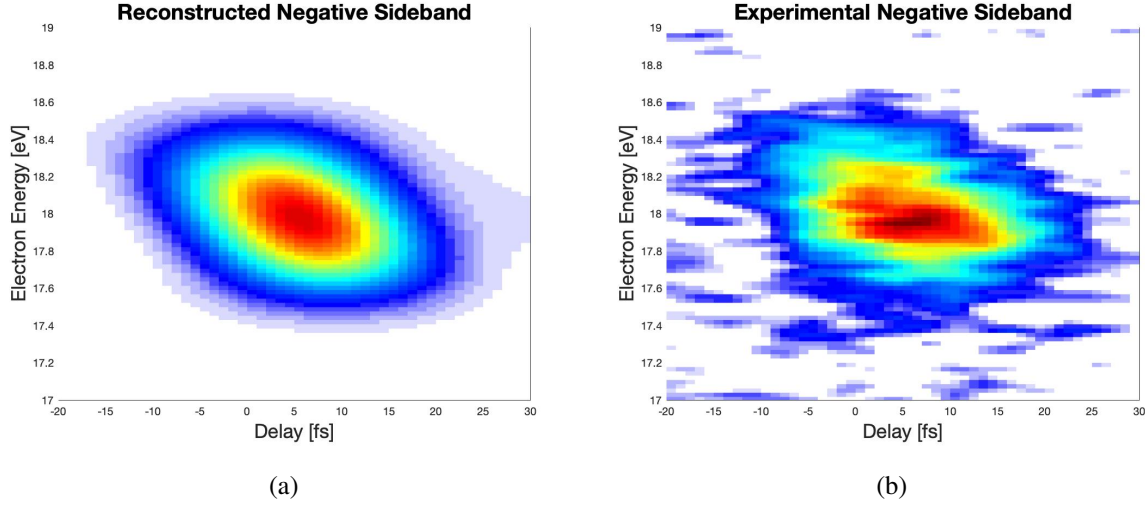
Figure 4.9: (a) Reconstructed negative sideband with STRIPE algorithm. The very bad tilt and stretch is no longer present, (b) Experimental reference negative sideband.

A way to check if an improvement took place is to compute the tilt of the sideband with a linear fit and compare it with the previous case. This can be done by computing the energy center of mass of the sideband and compare it with the one of the reference experimental sideband. The energy center of mass is defined as a vector $CM = (cm_1, cm_2, ..., cm_m)$ whose elements cm_i are calculated as:

$$cm_i = \sum_{\varepsilon_{i,j}^k = \varepsilon_1}^{\varepsilon_n} \varepsilon_{i,j}^k \cdot I_{i,j} \qquad (4.7)$$

Here the index i identifies a point in the delay axis, the index j a point in the energy axis, ε^k is the value of the kinetic energy and I is the value of the intensity. For every index i there is one value of the center of mass of the sideband at that precise delay. The fig.4.10 shows the fitted center of mass with a linear model for two different cases: one before the FWHM reduction fig.4.10b and the other after fig.4.10a. It is evident that the tilt is much better in the case of the FWHM reduction.
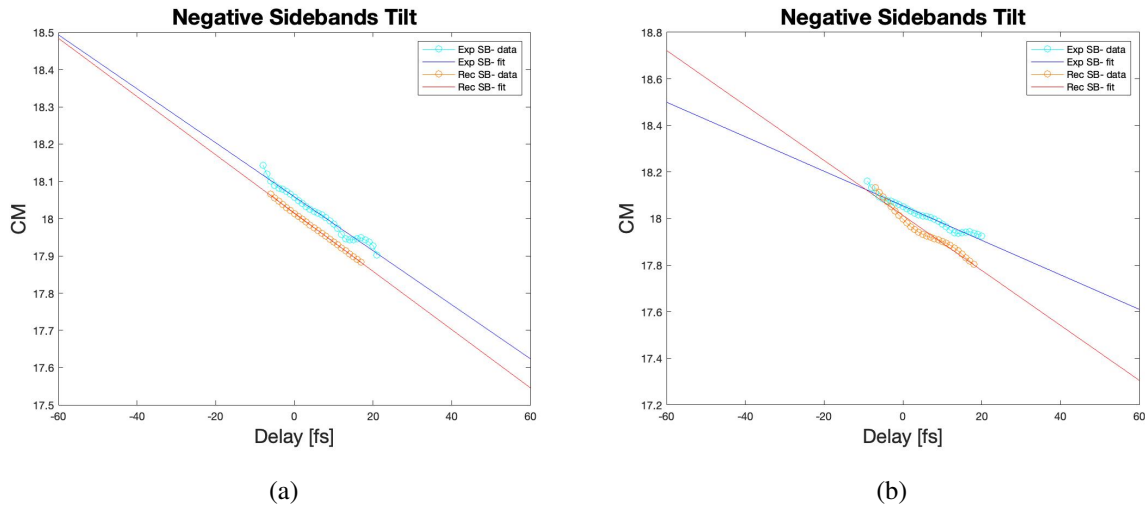
Figure 4.10: (a) Computed CM of the negative sideband after the FWHM reduction, (b) Computed CM of the negative sideband before the FWHM reduction.

All these evidences brought to the conclusion that the XUV spectrum employed until now could no longer be used: Indeed, even if the reconstruction of the sidebands after the changes explained above is promising, it is based on fictional data due to the manual modifications it was subjected to. These imperfections could be related to an undesired interaction between the XUV and UV pulses generating a broadening of the spectrum. A solution to this important issue was found in exploiting the photoelectron spectrum generated argon from the XUV pulse shown in fig.4.2.

Eventually is important to point out that due to the issues explained above the results shown here were obtained with a FWHM of the impulse response function with a value around the 0.1 eV, so too big to be significant for the study. Other values returned worse results, this consideration is important to underline that the process explained above is meant to be an analysis of the issues encountered and not a presentation of important results.

4.3.2 Final Pulses Reconstruction

After all the tries presented above a final reconstruction was obtained. The initial parameters in input to the STRIPE algorithm are are those reported in the table 4.1 with units as listed in the section 4.3.

λ_0^{UV}	275
UV BW	0.1
UV constant phase	$-(0.7\pi)$
UV GDD	50.0
UV TOD	0
UV FOD	0
UV intensity	1
XUV amplitude	10
XUV constant phase	0
XUV first order term	-4
XUV GDD	25
XUV TOD	0

Table 4.1: Input values of the final reconstruction referring to the units listed in the section 4.3

λ_0^{UV}	268
UV BW	0.1
UV constant phase	-3.142
UV GDD	20
UV TOD	-200
UV FOD	-4.908
UV intensity	1
XUV amplitude	7.260
XUV constant phase	-3.080
XUV first order term	-5.823
XUV GDD	32.937
XUV TOD	46.311

Table 4.2: Output values of the final reconstruction referring to the units listed in the section 4.3

With these initial guesses the code finds the minimum with the *lsqnonlin* with a few cycle with very good values for the *StepTolerance* and the *OptimalityTolerance* which represents a great step up with respect to the previous cases where the convergence was never this fast neither this good. The output parameters computed by the STRIPE algorithm are those reported in the table 4.2 with units as listed in the section 4.3.

The trace of the reconstructed positive sideband is reported in fig.4.11a.

(a)   (b)
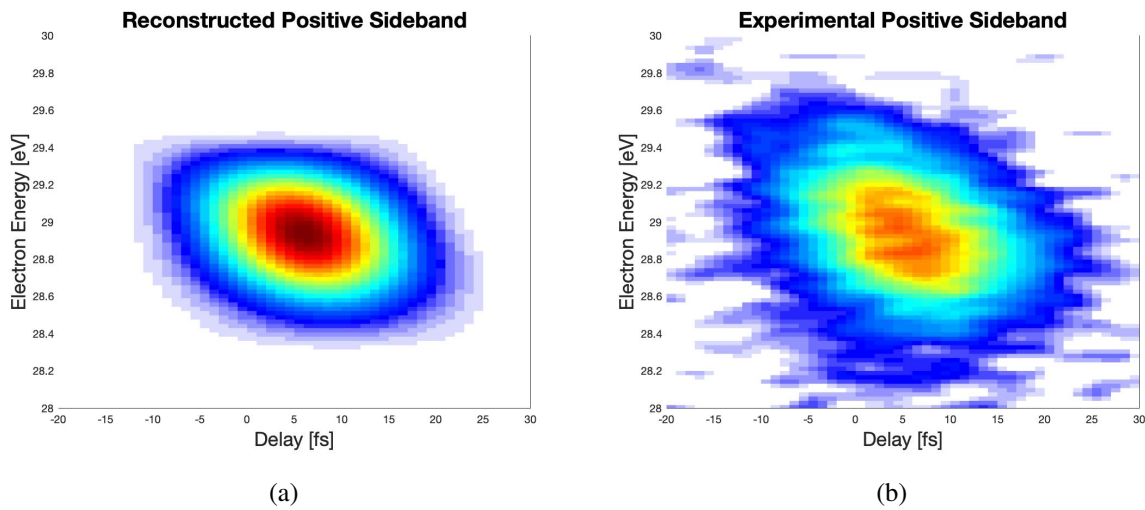
Figure 4.11: (a) Reconstructed positive sideband with STRIPE algorithm, (b) Experimental reference positive sideband.

To check the quality of the centering two types of integrals can be computed: the sum along the delay axis for the energy centering and the sum on the energy axis for the delay centering, both with respect to the experimental sideband. They are reported in fig.4.12 and show a good centering in both cases.
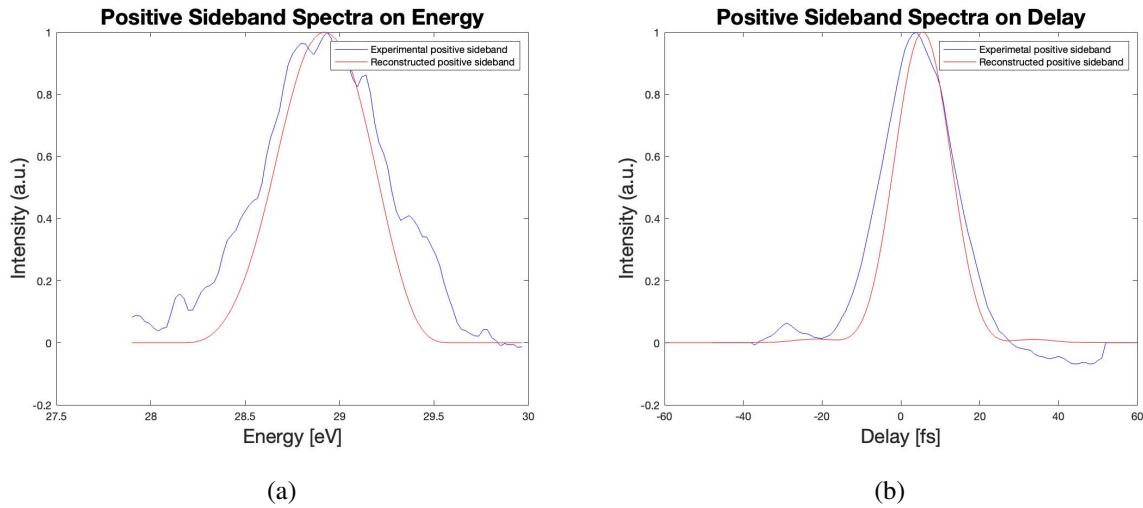
Figure 4.12: (a) Spectrum of the positive sideband resulting from the integration along the delay axis, (b) Integration along the delay energy axis to show the centering on delay of the positive sideband.

The trace of the reconstructed negative sideband is reported in fig.4.13a.
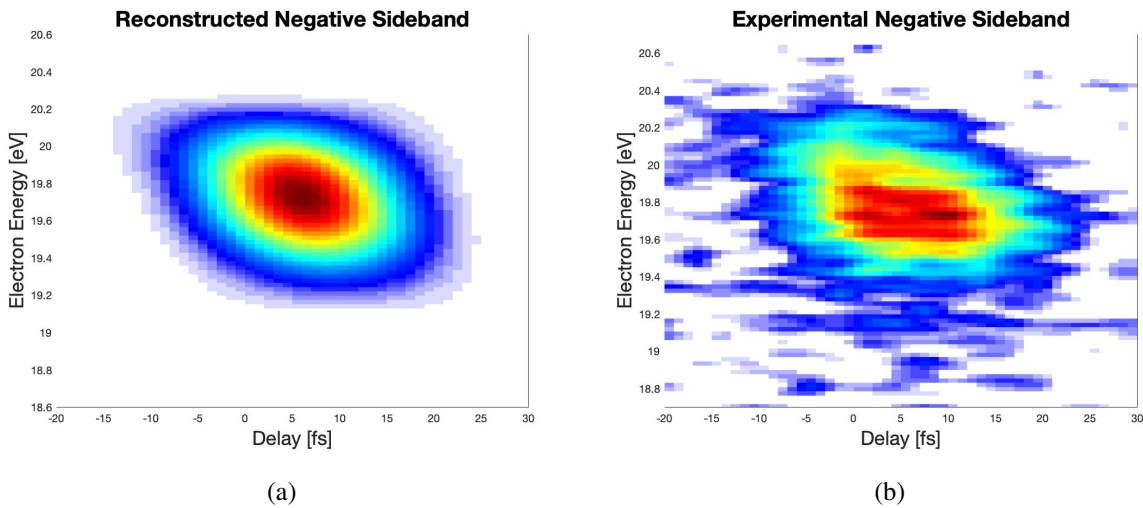
Figure 4.13: (a) Reconstructed negative sideband with STRIPE algorithm, (b) Experimental reference negative sideband.

The analog integrals for the negative sideband are reported in fig.4.14, showing again a good matching.
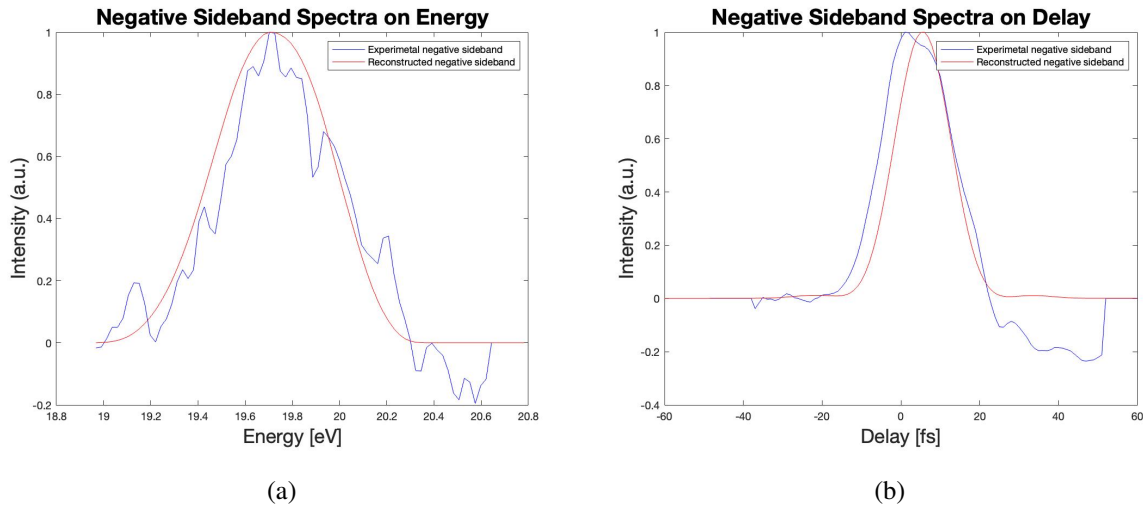
Figure 4.14: (a) Spectrum of the negative sideband resulting from the integration along the delay axis, (b) Integration along the delay energy axis to show the centering on delay of the negative sideband.

Eventually the computed and fitted center of mass in both cases is showed in fig.4.15.
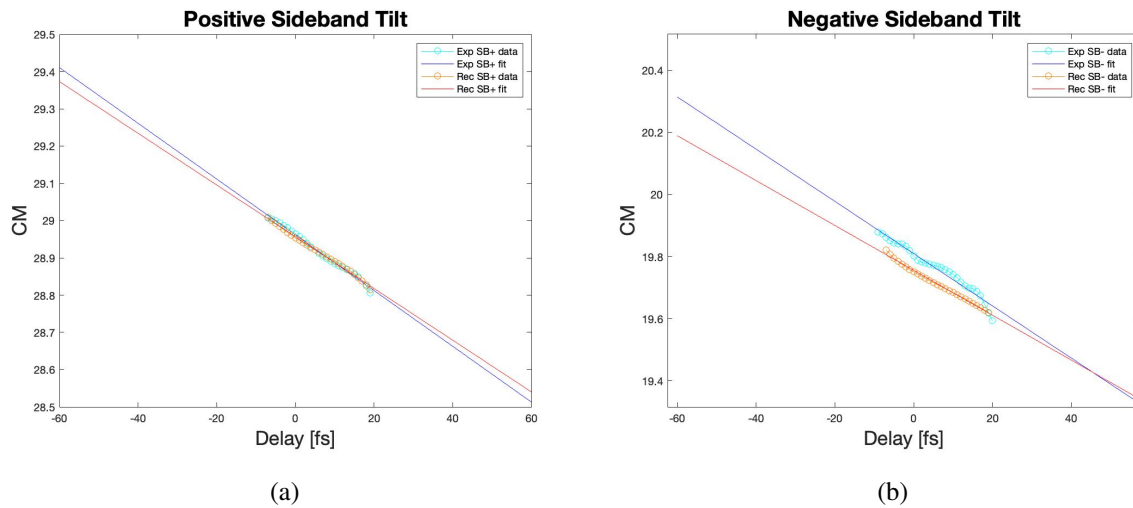
Figure 4.15: (a) Computed CM of the positive sideband, (b) Computed CM of the negative sideband.

In the positive case the the angular coefficient of the linear fit for the tilt of the center of mass is equal to -0.0075 for the experimental one and -0.0069 for the reconstructed case. This gives

a relative error of 7.6%. In the negative case the experimental angular coefficient is -0.0082 and the reconstructed one -0.0072, so a relative error of 12%.

Eventually the computed XUV and UV pulses in the time domain are shown in fig.4.16.
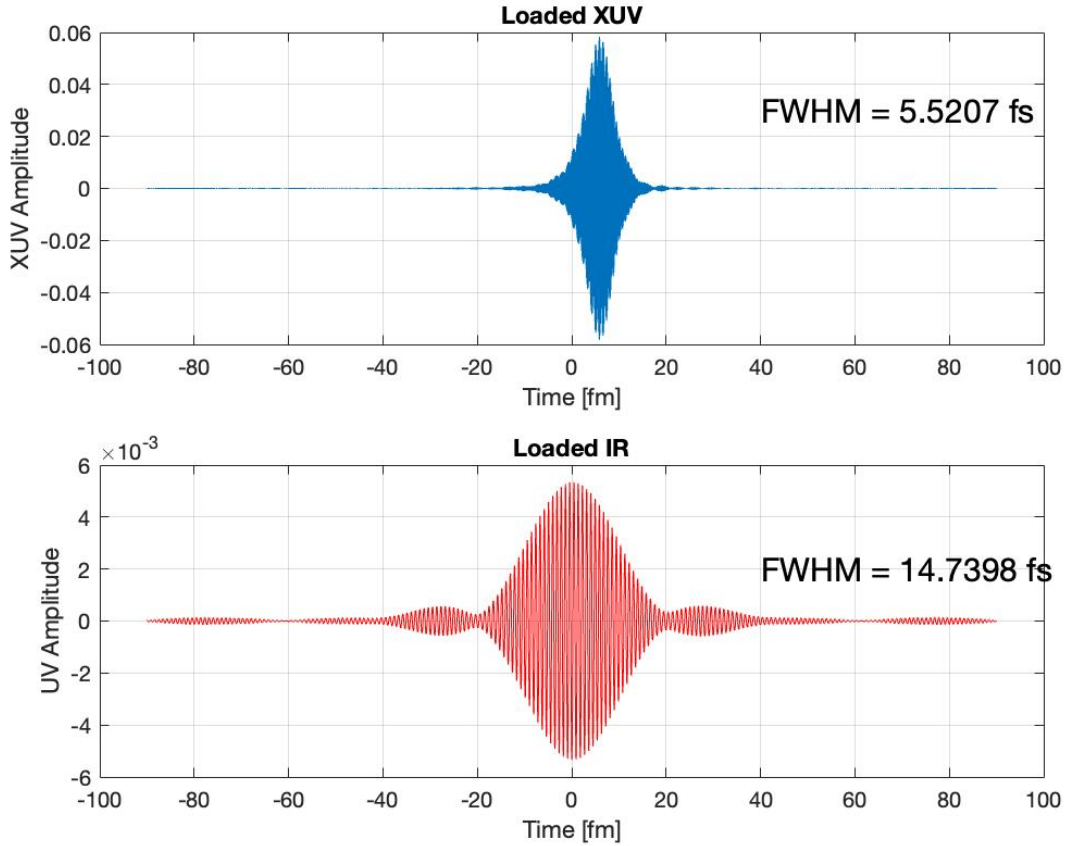
Figure 4.16: Reconstructed XUV and UV pulses in the time domain.

The FWHM of the pulses was computed by extracting their envelope through the Hilbert transform. A gaussian fit is performed on both the pulses envelope providing a precise estimate of the σ, the FWHM of the pulses is then computed as:

$$FWHM = 2\sqrt{2ln(2)}\sigma \qquad (4.8)$$

providing a value of 6 fs for the XUV and 15 fs for the UV.

5. Pump and Probe Spectroscopy on 2,6-Dimethylpyridine

This chapter is dedicated to the second part of the work and one of the most important practical applications of the attosecond science: the study the electronic dynamics in a molecule.

5.1 Dark Structures in Pyridines

Pyridine C_5H_5N is a *heterocyclic organic compound*, meaning it is a cyclic compound that has atoms of at least two different elements as members of its ring (heterocyclic) [1], carbon and nitrogen. It is structurally analog to benzene except for one methine group replaced by a nitrogen atom as shown in fig.5.1. Pyridine and its methyl derivatives are relevant molecules, which have attracted a great deal of attention over the last two decades [10] [73] [69] [52] due to their important roles in the UV photodamage of nucleic acids [12].
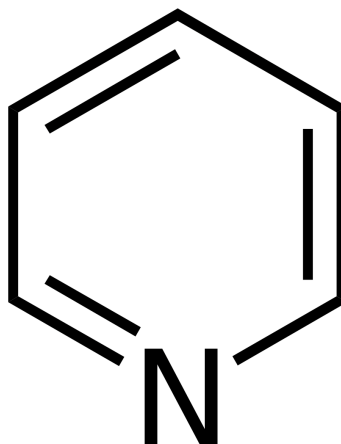
Figure 5.1: Molecular structure of pyridine.

Photoexcited polyatomic molecules often exhibit quite complex dynamics involving the redistribution of both charge and energy. Their dynamics is often dominated by non-adiabatic coupling of vibrational and electronic degrees of freedom, therefore they are described outside the Born-Oppenheimer approximation which is not valid. As a consequence the dynamics which take place lead to coupling of potential energy surfaces and extend nuclear motion to more than

one Born-Oppenheimer potential energy surface [51]. These processes are called radiationless transitions, electronic relaxation or internal conversion and are the primary steps in the photochemistry of many polyatomic molecules and photobiological processes such as vision and photosynthesis and underlie many concepts in molecular electronics [57]. Non-adiabatic coupling often leads to complex, broadened absorption spectra because of the high density of nuclear states and strong variations of transition dipole with nuclear coordinate. In this framework the ultrafast pump and probe spectroscopy represents a great tool which allows to investigate the radiationless decay of the photoionized molecule's initial state.

The intermediate structures formed through radiationless transitions are termed *dark* because their existence is inferred indirectly from radiative transitions. In aromatics such as benzenes and pyridines, upon absorption of light, a substantial portion of the energy is directed into non-radiative pathways. In particular, after light absorption, a molecule can undergo radiationless processes of two general types: *photochemical*, involving bond fragmentation or isomerization (process in which a molecule is transformed into an isomer with a different chemical structure) and *photophysical*, involving transitions between electronic states (with conservation or change of the spin) [56].

The existence of different radiationless transitions and therefore different dark structures implies the possibility that modifications in the structure of the molecule could result in a change of the molecule's behaviour once it is photoexcited. This has been experimentally demonstrated in the case of pyridine and some of its methyl-substituted derivatives [56] [51] [71]. Two simple derivatives are 2-methylpyridine and 2,6-dimethylpyridine presenting respectively one methyl group and two methyl groups substitutions. In [56] it is reported how, upon 266 nm excitation, pyridine and 2-methylpyridine undergo C–N bond scission to open the aromatic ring and form a diradical structure. The ring opening process is not uncommon and there are other examples of molecules with such behaviours like 1,3 cyclohexadiene C_6H_8 [13]. Indeed an excitation of the molecule, e.g. through a UV pulse, can bring the molecule in such a state that does not represent an advantage from the energetic point of view with respect to the open ring configuration. As a consequence the molecules relaxes towards a lower energy configuration represented in this case by the open ring scheme. However as mentioned above, this is not the only possibility and the case of 2,6-dimethylpyridine shows another possible path in the evolution of the excited

molecule. This specific case is studied and illustrated in the section 5.4 of this chapter.

5.2 Methodology

One of the most extended schemes in VUV-XUV spectroscopy science is time-resolved photo-electron spectroscopy, borrowed from the attosecond science. This technique involves a first pulse (pump), which drives the system out of equilibrium, and a second pulse (probe), which follows the dynamics initiated by the pump. This process can typically involve an XUV attosecond pulse in combination with an intense few-cycle IR field, but in the present work a pump UV and probe XUV were employed. The UV pulses are used to bring the molecule in an excited state and the XUV to extract the photo-induced dynamics information by looking at the emitted photoelectron. There exists a large variety of techniques to obtain spectroscopic information from the electrons released upon the induced photoionization. One of the most widespread methods is the use of time of flight (TOF) spectrometers, which measure the time required by a charged particle to fly along a drift tube, allowing to obtain the kinetic energy distribution of the photoelectrons [8]. As explained in the chapter 3 this is exactly the solution adopted for the present work.

In the present case a pump (UV centered around 270 nm) and probe (XUV centered around 38.75 eV) experiment was performed on molecules of 2,6-dimethylpyridine shown in fig.5.2.
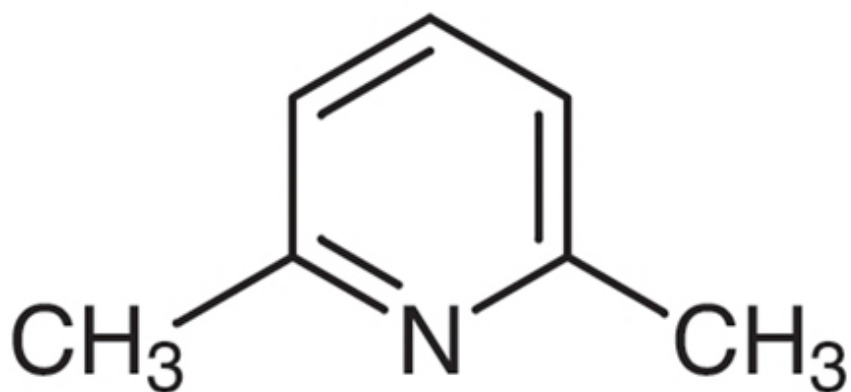
Figure 5.2: Molecular structure of 2,6-dimethylpyridine.

5.3   Data

The method explained in the section 5.2 provides as a result a photoelectron traces like the one in fig.5.3 which is obtained from 2-methylpyridine.
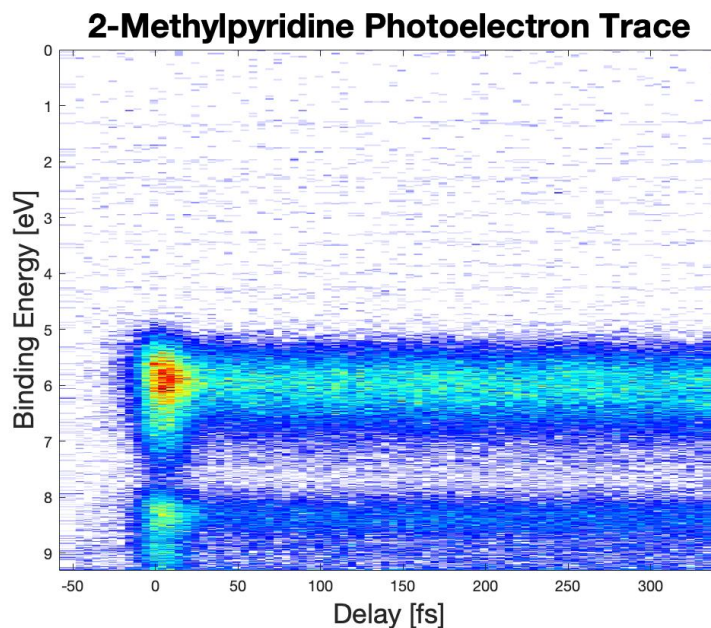
Figure 5.3: Photoelectron trace of 2-methylpyridine.

2,6-dimethylpyridine $(CH_3)_2C_5H_3N$ is pyridine derivative with methyl groups substitutions, therefore it has a cyclic structure with π bonds in resonance, those containing delocalized electrons [33].

Two different kinds of photoelectron traces were collected. The first can be labelled as *High Resolution Scans* HS and is characterized by a smaller delay axis range explored between the UV and the XUV pulses with a resolution of 5 fs. The other one presents a wider delay axis range with a step of 25 fs between one point and the next one, those are called *Low Resolution Scans* LS. The choice of collecting two different kinds of scans is due to the fact that with a higher resolution is possible to study dynamics with shorter characteristic times, while a wider range of delays can contain an interesting evolution which could require even hundreds of *fs* to take place and be observed.

5.3.1   Data preparation

Working on a single measurement is almost never a good way to proceed in this field, so the collection of a acceptable statistic is necessary, not only to try to compensate the noise, but also solving issues related to different conditions in which the measurements were performed. This brings some issues that have to be faced with a pre-processing of the data. Indeed, the time required to measure one scan of a trace is such that it didn't allow to collect much per day. Moreover, by the time required to perform one measurement, some conditions on the setup could change and not be equivalent for the next one.

The first essential step is the calibration of the energy axis in the traces. Analogously to what happens in the case of the sideband reconstruction the TOF spectrometer returns scans without an axis in energy, but in pixel positions. This means that subject to a measurement of a reference spectrum with known peaks, the conversion can be performed through the functions in eq.4.4 and 4.5. This procedure is done for each scan keeping in mind that different scans could be coupled with different reference spectra.

Once the calibration is completed the energy axes of different traces could present an offset and therefore not be aligned. This could be particularly relevant in the case they were collected in different days. To solve this issue a relevant feature of the traces can be identified, like a main band or a clear signal of photoelectron. These features have to correspond to the same energies values since the system studied is the same, so we expect the same physical process to take place.
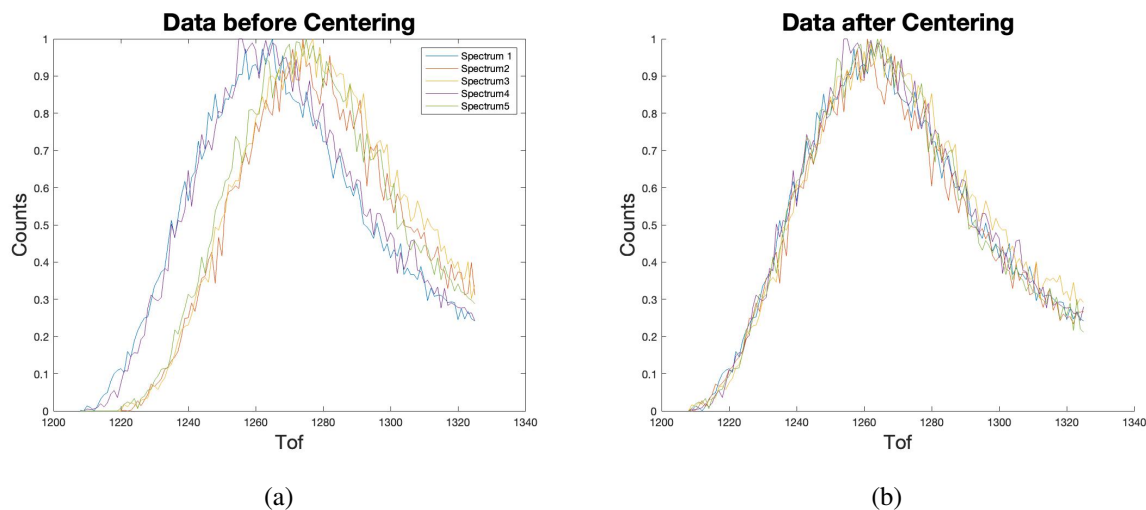
Figure 5.4: (a) Spectra computed before the centering of the photoelectron trace, (b) Spectra computed after the centering of the photoelectron trace.

After an integration on the delays axis to obtain a spectrum on the energy, typically gaussian shaped, a centering can be performed between all the traces to obtain the best superposition. The same process has to be applied to the delay axes of different scans, taking as reference feature for example the rising of a signal. In fig.5.4 an example of this process is reported. The fig.5.4b contains the centered spectra after the shift computed with the gaussian fit.

After these processes the traces can be finally averaged to obtain a single on both in the HS and LS cases.

5.4 Results

The two cases of the HS and the LS are here analysed separately.

5.4.1 High Resolution Scans HS

The HS of 2,6-dimethylpyridine is showed in fig.5.5.

Figure 5.5: Photoelectron trace of 2,6-dimethylpyridine.

Looking at the fig.5.5 it seems that no remarkable relaxing process is taking place, however a deeper analysis shows this kind of dynamic. First of all let's see how the energy center of mass $CM = (cm_1, cm_2, ..., cm_m)$ behaves. It is defined as in eq.4.7. The result is reported in the plot in fig.5.6 as center of mass vs delay between the two pulses.
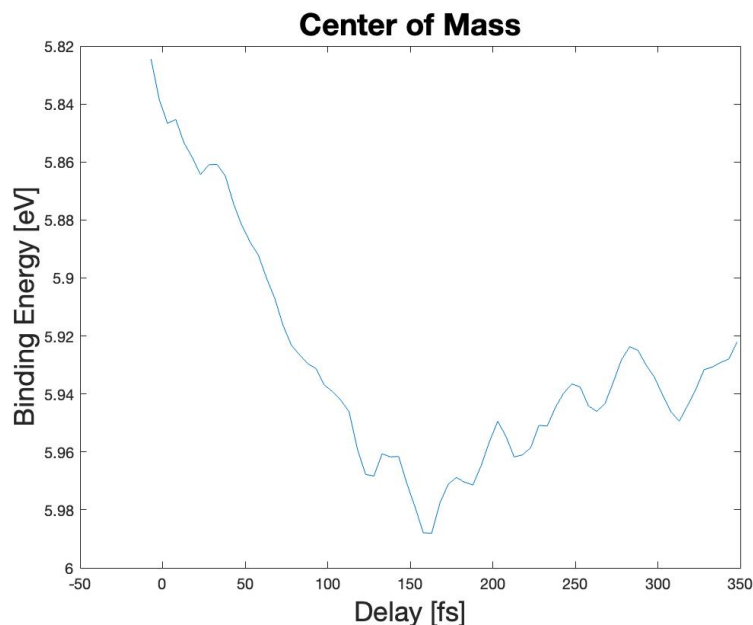
Figure 5.6: Energy center of mass of 2,6-dimethylpyridine signal.

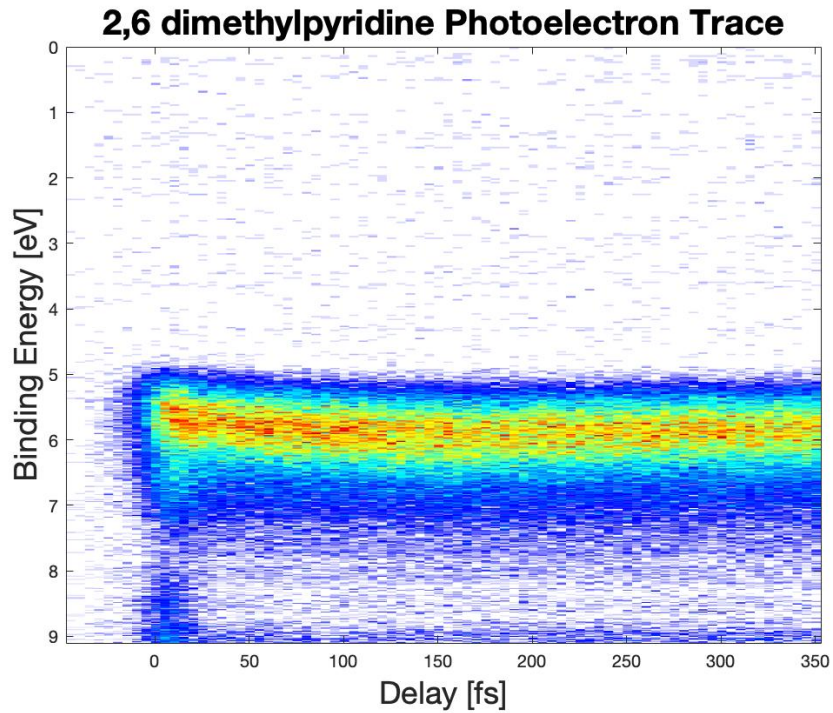Within the first 150 fs a relaxation takes place with an energy variation of about 0.15 eV. After hitting the minimum around 160 fs a smaller rise starts. Various models were tried to find a good fit for this general dynamic, the best one was found by considering the same plot tipped over along the energy axis. In this case the model used was the following:

$$f(x) = c_1 e^{\frac{-(x-c_2)^2}{2c_3^2}} + c_4 \left[1 + erf \left(\frac{x - c_2}{c_3} \right) \right] \cdot e^{-\frac{x-c_2}{c_5}} \tag{5.1}$$

where $\boldsymbol{c} = (c_1, c_2, c_3, c_4, c_5)$ are the parameters of the fit and erf is the MATLAB error function, c_1 representing the gaussian amplitude, c_2 the center of the gaussian, of the error function and the decaying exponential, c_3 the gaussian σ, c_4 the the error function amplitude and c_5 the characteristic decay time of the exponential. The result of the fit is showed in fig.5.7. The dynamics that follow the rise after the first 300 fs will be analysed with longer delay ranges in the section 5.4.2. Within this shorter range the relaxation process is well visible and can be reconstructed with the fit.

Figure 5.7: Fitted energy center of mass of 2,6-dimethylpyridine signal.

The characteristic time of the first relaxation is computed as the FWHM of the σ of the gaussian in eq.5.1. The result provides a value of about 160 fs. As explained in section 5.1, the decay processes can be attributed to different physical phenomena, however in the same section it was observed how fo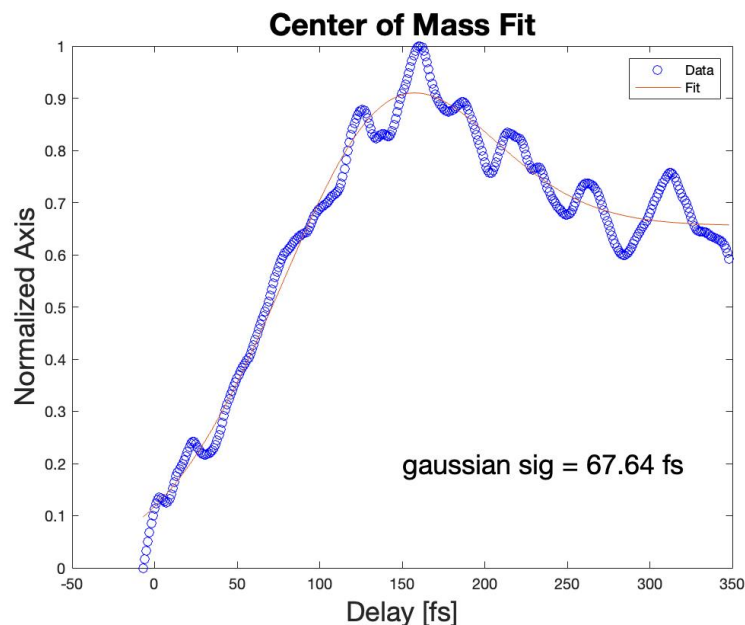r pyridines the ring opening reaction is not uncommon. As a matter of fact, within this framework, it is a typical evolution for pyridine and 2-methylpyridine. In the case of 2,6 dimethylpyridine excited by a UV at about 268 nm the dynamic taking place has a different nature. The methyl substitutes groups have a fundamental role in this. Upon methyl substitution, the electron-donating nature of these groups increases the electron density on the ring, leading to greater stability [49]. The presence of a single methyl substitute group does not produce a stabilization large enough to prevent the ring opening reaction in the 2-methylpyridine, but in 2,6 dimethylpyridine this is exactly the case. As suggested in [56] the nonradiative process we are witnessing is photophysical internal conversion, referring to the distinction made in section 5.1. In particular they suggest that 2,6 dimethylpyridine undergoes a *hot transition* which means a transition between two excited vibrational states of the molecule. This transition can end up exciting a normal mode of the ionized molecule and give rise to coherent oscillations. The analysis of the dynamic which follows the relaxation process discussed above can potentially reveal such behaviours.

Focusing on the delay values longer than 110 fs, the rising part of the signal in the plot in fig.5.6, some oscillations appear to characterize the behaviour of the dynamic. They can be studied both as oscillations in the intensity of the photoelectron signal and variations in the energy center of mass to have a more general picture. In fig.5.8 are reported the oscillations of the intensity of the photoelectron signal. The plot is obtained as sum of the intensity values for each delay in the range of interest of the signal. To analyse only the oscillation without the contribution of the decay, the oscillations obtained were smoothed and the result was employed as a baseline and therefore subsequently subtracted from the original plot. This generates oscillations that are on average centered around the zero of intensity as reported in fig.5.8.
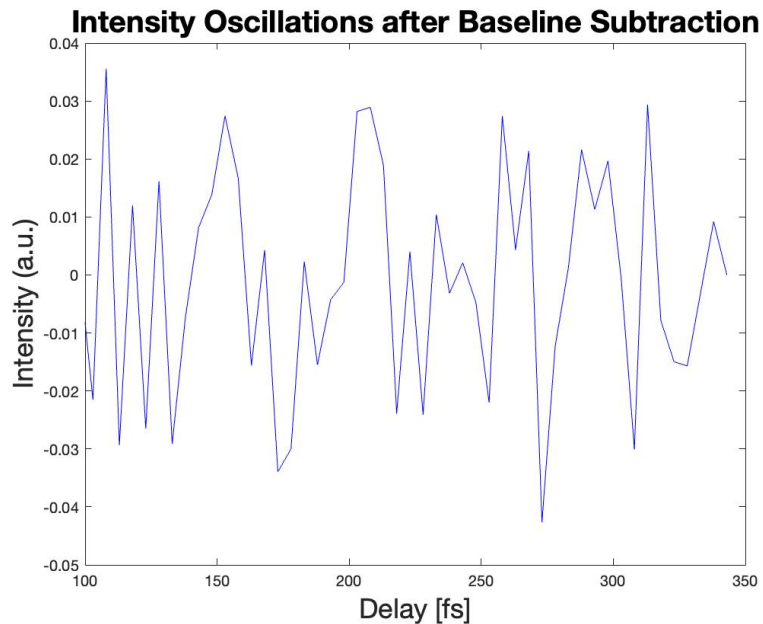
Figure 5.8: Oscillations of the intensity of the photoelectron signal after baseline subtraction.

From this picture it is impossible to verify the presence of coherent oscillations, for this reason it is necessary to go to the frequency domain through the Fourier transform. First of all a zero padding was exploited to obtain a better frequency resolution and the Hann window was applied to improve the accuracy of the calculations. The power spectrum computed as the square of the absolute value of the F.T. of the oscillations is showed in fig.5.9.
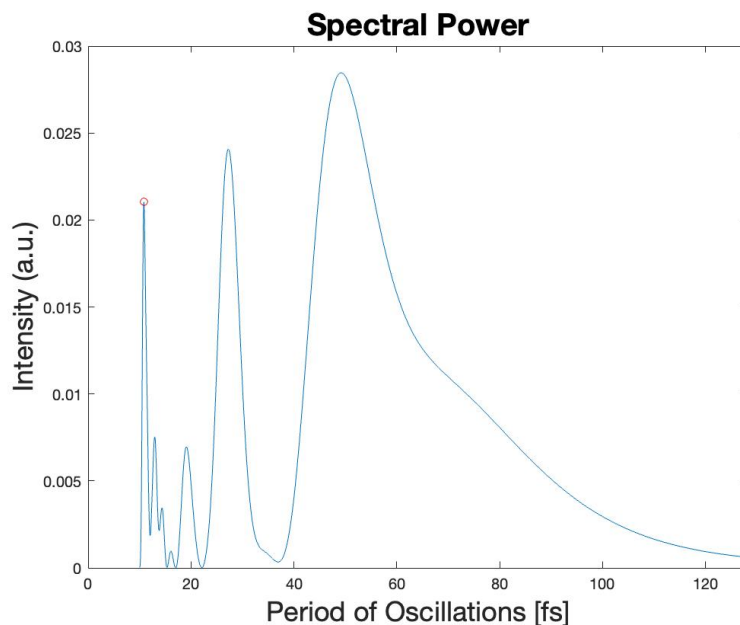
Figure 5.9: Power Spectrum of oscillation in intensity.

From the plot emerges the presence of coherent oscillations as suggested before. The greatest contribution is found for a value of about T=48 fs, so quite fast oscillations that would be difficult to distinguish from the noise in the case of LS, since they have a resolution of 25 fs. Another important contribution at about 27 fs a value that would almost coincide with the resolution in the case of LS. The use of two different approaches such as HS and LS can now be appreciated and understood more. The oscillations before this range can be associated with noise, it would be unsafe to link them to molecule oscillations given the resolution of 5 fs we are currently working with.

The same process was applied to the oscillation of the energy center of mass showed in fig.5.10.
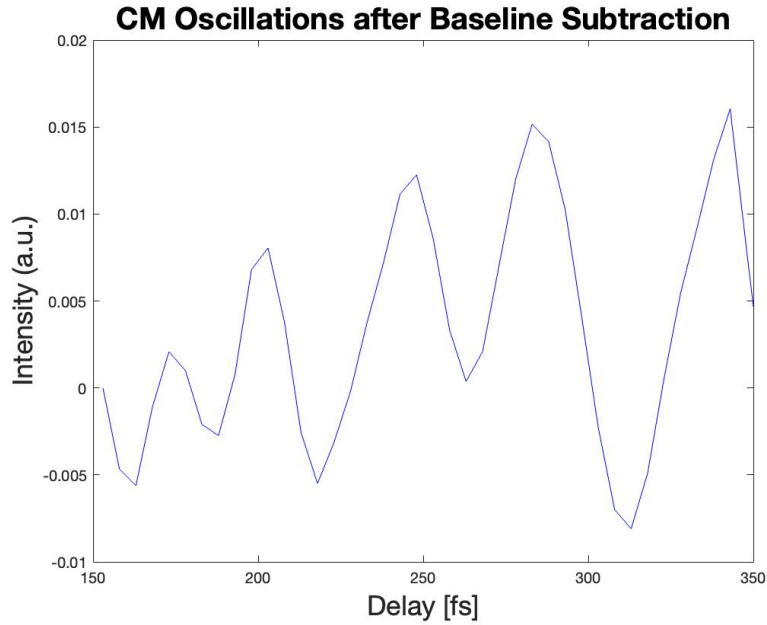
Figure 5.10: Oscillations of the energy center of mass of the photoelectron signal after baseline subtraction.

The power spectrum (fig.5.11 returns a peak in correspondence of a period with a value close to the one present in the oscillations of the only intensity.
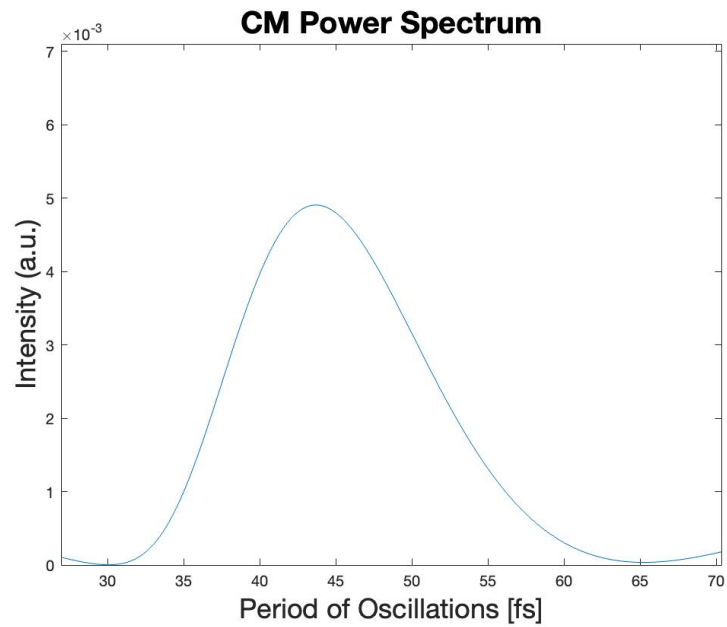
Figure 5.11: Power Spectrum.

5.4.2 Low Resolution Scans LS

The LS of 2,6-dimethylpyridine is showed in fig.5.12.
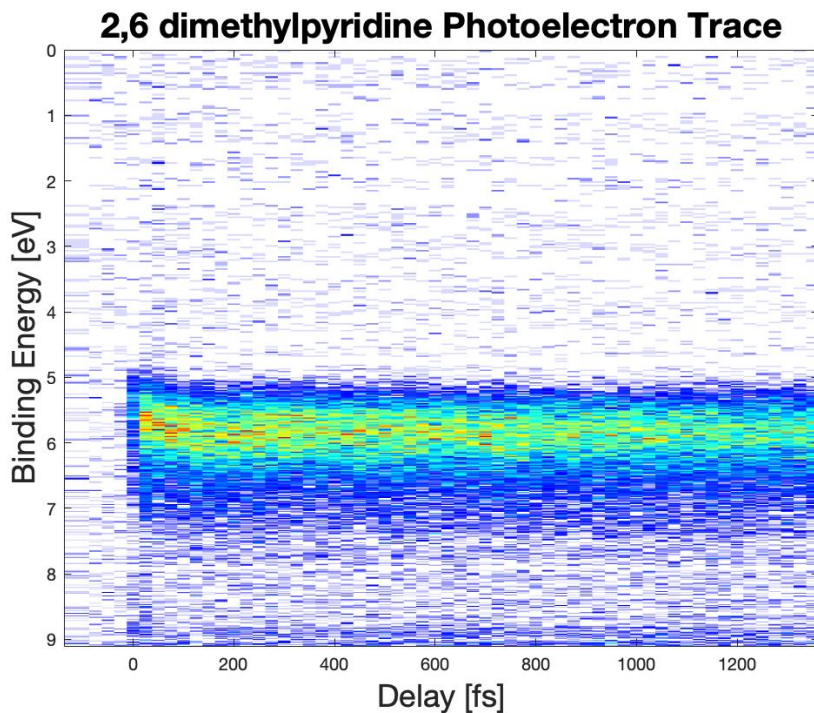
Figure 5.12: Photoelectron trace of 2,6-dimethylpyridine for LS.

As in the case of the HS there is no presence of two clear signals representing the status of the molecule before and after the excitation. However focusing on the band of the signal and computing the energy center of mass it can be seen a clear decay in the energy as showed in fig.5.13. The energy variation of the decay within the first 150 fs is about 0.15 eV, that is the same observed with the HS. This result is coherent and can be compared to the previous case since the range of delays is exactly the same, the difference is that the LS lacks in resolution. However for such a long dynamic it does not represent a limitation.
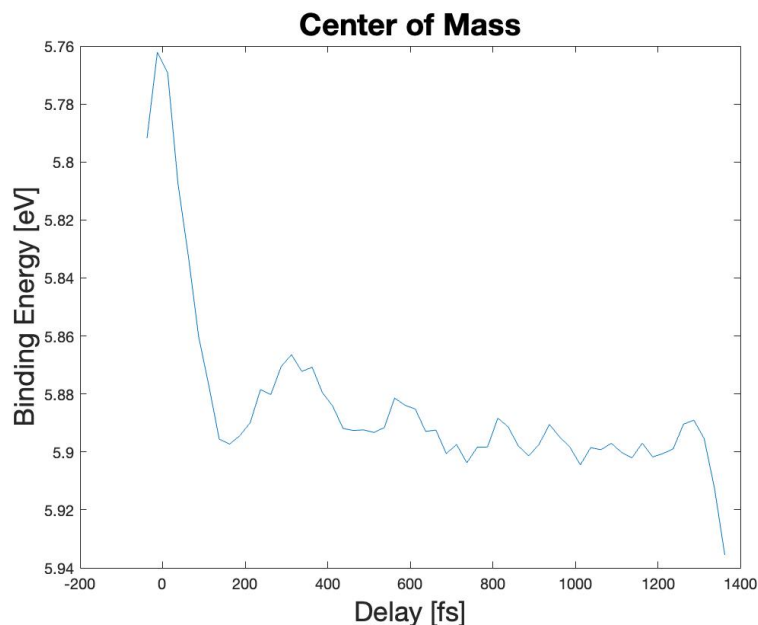
Figure 5.13: Energy center of mass of 2,6-dimethylpyridine signal for LS.

In the previous section 5.4.1 we showed how the relaxation dynamic observed in this initial part of the plot can be led back to a transition into a different vibrational state after the UV excitation, called hot transition. The LS can be used to study the initial decay seen in fig.5.13 and find its characteristic time.

The same fitting function as the one in eq.5.1 is employed also in for the plot in fig.5.13, but without the need of tipping over the spectrum. The result is showed in fig.5.14. In this case the FWHM of the gaussian does not correspond to the same as the one computed for the HS. In the HS case the spectrum was tipped over, so the gaussian represented a minimum of the CM value, a process which included the initial decay and the subsequent rise of the CM. In the LS case an analog fit could be made, but it would be less precise and reliable, Indeed, as emerges from fig.5.13 the above mentioned dynamic takes place within less than one tenth of the delay range in the LS plot, therefore it is much more convenient to study it with the HS. Focusing on the decay process at the beginning of the dynamic, the FWHM computed with the σ of the fit is eventually equal to about 120 fs.
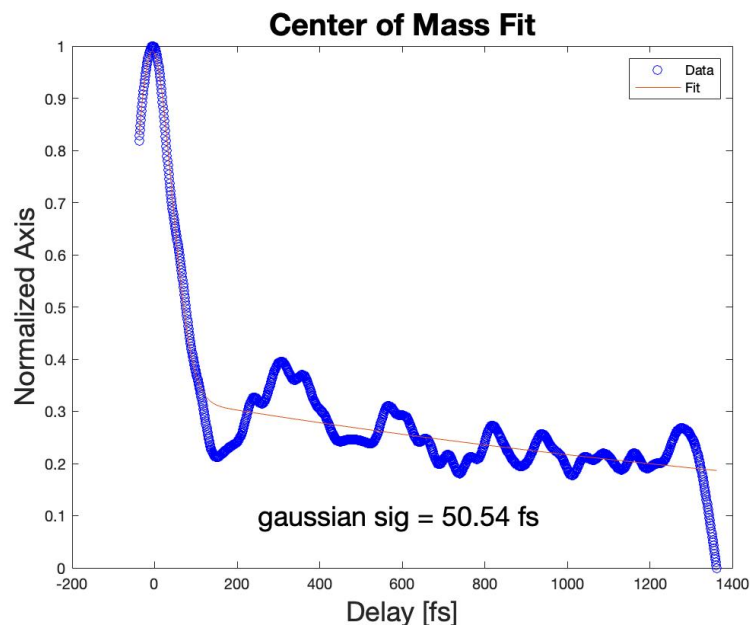
Figure 5.14: Fitted energy center of mass of 2,6-dimethylpyridine signal.

As mentioned, the minimum showed in fig.5.14 around 170 fs corresponds to the minimum showed with a much better resolution of 5 fs in fig.5.6. As a consequence this faster dynamic and all the oscillations present in the HS case can not be studied for the LS with a resolution of 25 fs. Nonetheless from these data it is possible to extract information about dynamics with longer characteristic times which could represent longer coherent oscillation of the excited vibrational state, not visible with HS. In fig.5.14 after the initial big decay, one slower and smaller decay towards lower energies is visible. It can be evaluated with the characteristic time of the decaying exponential in eq.5.1 as reconstructed by the fit. The value obtained is τ=2.5 ps, however for such a long dynamic, way beyond the femtosecond duration, a longer scan would be needed to analyse it in its full evolution and get rid of all the possible factor that interfere with it. As a matter of fact the estimated value is a longer time than the one available in the whole delay range, so this single derivation has to be considered not too rigorously.

Regarding the study of the longer oscillations in the fig.5.13, the same method of the Fourier analysis can be applied both to the intensity and the energy center of mass variations in time, as seen in section 5.4.1. In fig.5.15 it is reported the oscillation plot of the intensity after the baseline subtraction.
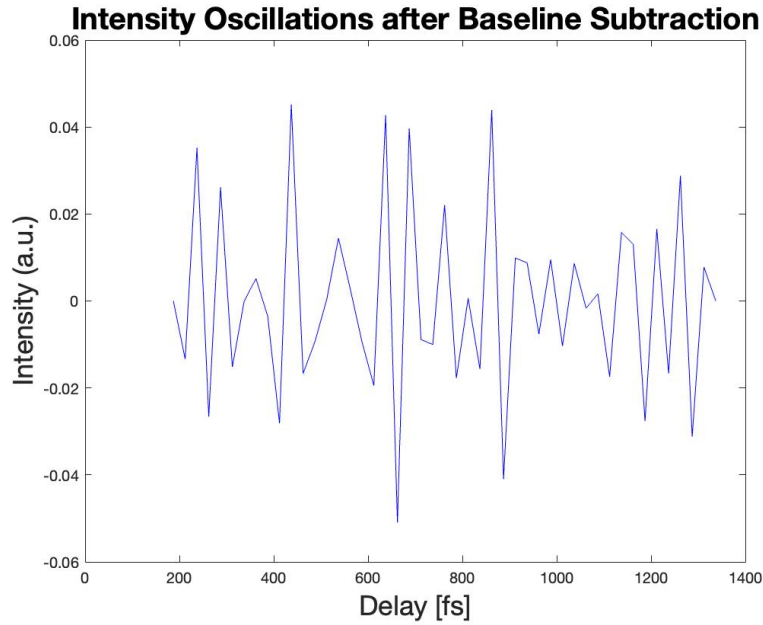
Figure 5.15: Oscillations of the intensity of the photoelectron signal after baseline subtraction.

After the Fourier analysis the power spectrum in fig.5.16 is obtained showing a relevant component around 100 fs, longer with respect to what was the focus in the case of the HS.
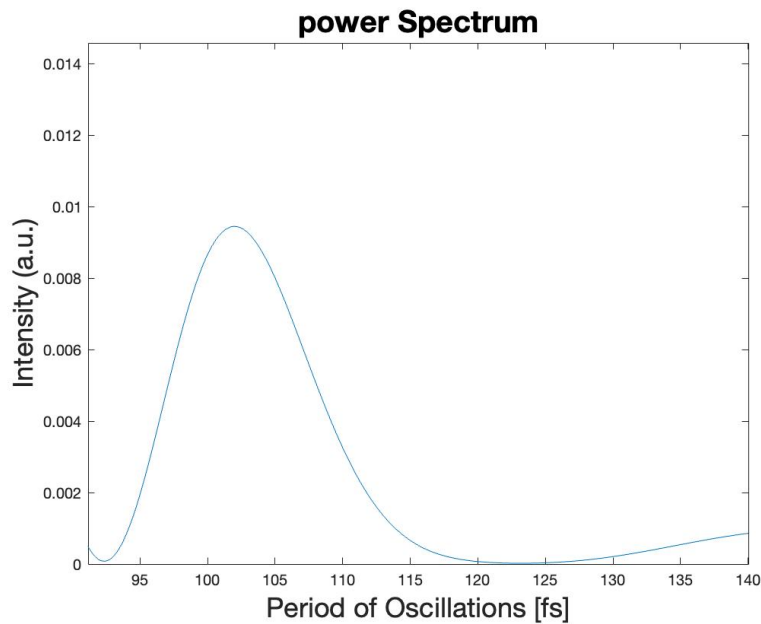
Figure 5.16: Power Spectrum of oscillation in intensity.

Regarding the oscillations of the energy center of mass reported in fig.5.17 a slower dynamic

was observed.
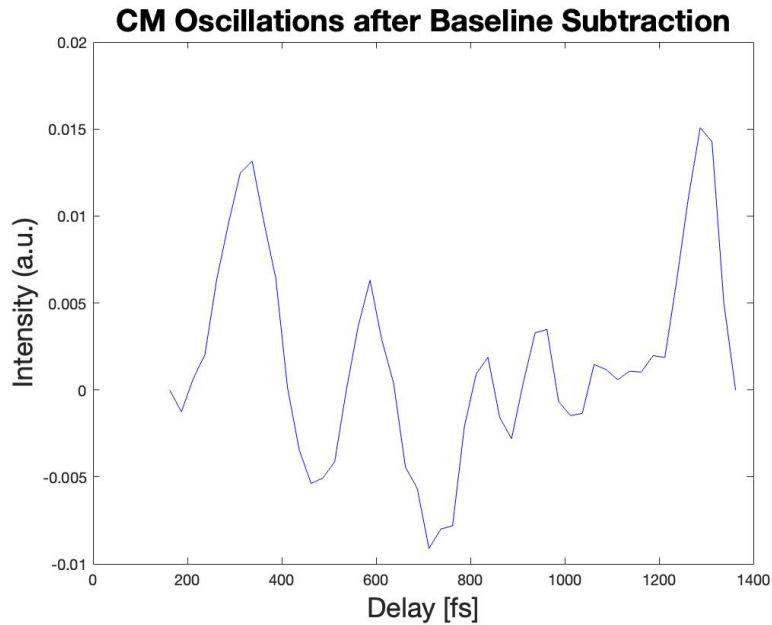
Figure 5.17: Oscillations of the energy center of mass of the photoelectron signal after baseline subtraction.
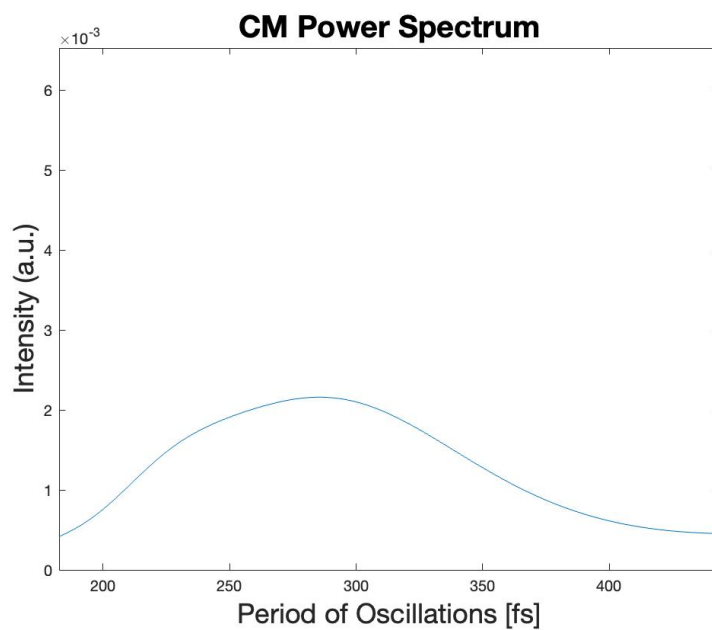
Figure 5.18: Power Spectrum.

Indeed in fig.5.18 the power spectrum shows oscillations with period in the range between

250 - 300 fs which is almost equal to the whole interval in which the this kind of dynamic was studied for the HS. This implies that in the SS case the longer oscillation was removed together with the baseline, the same thing is not happening for the LS where the time periods of hundreds of fs are clearly visible, but the tens of fs are hidden within them.

Conclusions

In this document, we have demonstrated one of the major applications of attosecond science, namely the study of electronic dynamics in 2,6-dimethylpyridine through a XUV probe signal once it was photoexcited by a UV pump signal.

The work was first introduced by a brief explanation of this research field and the technological and scientific advancement allowed by it. A simple, but efficient historical reconstruction of all the discoveries was presented starting from the 1960s till the early 2000s. We presented various innovations like the HHG, the femtosecond solid-state lasers and CEP control trying to highlight what each of them brought to the table and the steps forwards that followed them.

The attosecond science is a relatively recent field characterized by a certain degree of complexity when one tries to understand every piece that composes it, for this reason we presented a chapter dedicated to the fundamental theory at its basis. The HHG three step model was presented as it represents a simple theoretical description of what is the main process without which no XUV pulses would be generated and therefore no UV-XUV experiment could take place. The characterization of such pulses is another fundamental element of every experiment, therefore two of the most spread techniques for this scope were presented trying to provide both the formula at the basis, but also the physical principles they are based on.

Subsequently we showed the process of temporal reconstruction of the UV and XUV pulses. First of all we illustrated the issues with the initial data and the problems in the reconstruction they caused which brought to change the XUV photons spectrum with a photoelectrons spectrum. The reconstruction with the new data presented a much better performance with the STRIPE algorithm implemented in MATLAB. Other parameters were employed to check the quality of the result of the algorithm like the centering of the sidebands and their tilt. The final pulses were reconstructed finding a good duration of about 5 fs and 15 fs respectively for the XUV and the UV.

Lastly the analysis on the 2,6 dimethylpyridine is reported. After a brief description of the previous studies on pyridine and derivatives we provided a description on the methodology used

to obtain our data and the pre-processing that was needed before the actual analysis could take place. The results of the analysis are eventually showed, both for the short scan SS with a resolution of 5 fs and the long scan LS with a resolution of 25 fs. We reported the characteristic times of the relaxation process after the photoexcitation by the 268 nm UV pump of the molecule, explaining the fundamental difference in the nature of this evolution with respect to the other pyridine derivatives aforementioned. The hot transition that takes place in the case of 2,6 dimethylpyridine is explained with reference to previous works and the resulting coherent oscillations of the new vibrational state of the molecule are analysed. We pointed out precisely also the differences between the two kind of data represented by the SS and LS, since they provide different information on the same process, therefore showing the importance of exploiting both of them to obtain a more general picture of the phenomenon.

Appendix

Referring to the section 4.3 the MATLAB function *lsqnonlin* within the STRIPE algorithm responsible for the minimization as described in the mentioned section requires the definition of some parameters, otherwise set to the default MATLAB vales. In particular in the present work the following values were employed:

- MaxFunctionEvaluations (maximum number of function evaluations allowed) set to 10^6,

- FunctionTolerance (termination tolerance on the function value) set to 10^{-12},

- MaxIterations (maximum number of iterations allowed) set to 500,

- StepTolerance (termination tolerance on x referring to eq.4.6 set to 10^{-12},

- OptimalityTolerance (termination tolerance on the first-order optimality) set to 10^{-12}.

Bibliography

[1] Pragi Arora et al. "Importance of heterocyclic chemistry: a review". In: *International Journal of Pharmaceutical Sciences and Research* 3.9 (2012), p. 2947.

[2] A. Baltuška et al. "Attosecond control of electronic processes by intense light fields". In: *Nature* 421.6923 (Feb. 2003), pp. 611–615. ISSN: 1476-4687. DOI: 10.1038/nature01414. URL: https://doi.org/10.1038/nature01414.

[3] A. Baltuška et al. "Attosecond control of electronic processes by intense light fields". In: *Nature* 421.6923 (2003), pp. 611–615. DOI: 10.1038/nature01414. URL: https://doi.org/10.1038/nature01414.

[4] Aditi Bhattacherjee et al. "Ultrafast intersystem crossing in acetylacetone via femtosecond x-ray transient absorption at the carbon K-edge". In: *Journal of the American Chemical Society* 139.46 (2017), pp. 16576–16583.

[5] Jens Biegert et al. "Attosecond technology(ies) and science". In: *Journal of Physics B: Atomic, Molecular and Optical Physics* 54.7 (June 2021), p. 070201. DOI: 10.1088/1361-6455/abcdef. URL: https://dx.doi.org/10.1088/1361-6455/abcdef.

[6] N. Bigler et al. "High-power OPCPA generating 1.7 cycle pulses at 2.5 μm". In: *Opt. Express* 26.20 (2018), pp. 26750–26757. URL: https://www.osapublishing.org/oe/fulltext.cfm?uri=oe-26-20-26750&id=398370.

[7] Cosmin I. Blaga et al. "Strong-field photoionization revisited". In: *Nature Physics* 5.5 (2009), pp. 335–338. ISSN: 1745-2481. DOI: 10.1038/nphys1228. URL: https://doi.org/10.1038/nphys1228.

[8] Rocío Borrego-Varillas, Matteo Lucchini, and Mauro Nisoli. "Attosecond spectroscopy for the investigation of ultrafast dynamics in atomic, molecular and solid-state physics". In: *Reports on Progress in Physics* 85.6 (2022), p. 066401.

[9] Laura Cattaneo et al. "Comparison of attosecond streaking and RABBITT". In: *Optics express* 24.25 (2016), pp. 29060–29076.

[10] Mirianas Chachisvilis and Ahmed H Zewail. "Femtosecond dynamics of pyridine in the condensed phase: Valence isomerization by conical intersections". In: *The Journal of Physical Chemistry A* 103.37 (1999), pp. 7408–7418.

[11] O. Chalus et al. "Mid-IR short-pulse OPCPA with micro-Joule energy at 100kHz". In: *Opt. Express* 17.5 (2009), pp. 3587–3594. DOI: 10.1364/OE.17.003587. URL: https://doi.org/10.1364/OE.17.003587.

[12] Carlos E Crespo-Hernández et al. "Ultrafast excited-state dynamics in nucleic acids". In: *Chemical reviews* 104.4 (2004), pp. 1977–2020.

[13] Sanghamitra Deb and Peter M Weber. "The ultrafast pathway of photon-induced electrocyclic ring-opening reactions: the case of 1, 3-cyclohexadiene". In: *Annual review of physical chemistry* 62 (2011), pp. 19–39.

[14] Benoît Debord et al. "Hollow-Core Fiber Technology: The Rising of "Gas Photonics"". In: *Fibers* 7.2 (2019). ISSN: 2079-6439. DOI: 10.3390/fib7020016. URL: https://www.mdpi.com/2079-6439/7/2/16.

[15] M. Drescher et al. "Time-resolved atomic inner-shell spectroscopy". In: *Nature* 419.6909 (Oct. 2002), pp. 803–807. ISSN: 1476-4687. DOI: 10.1038/nature01143. URL: https://doi.org/10.1038/nature01143.

[16] U. Elu et al. "High average power and single-cycle pulses from a mid-IR optical parametric chirped pulse amplifier". In: *Optica* 4.8 (2017), pp. 1024–1029. DOI: 10.1364/OPTICA.4.001024. URL: https://doi.org/10.1364/OPTICA.4.001024.

[17] R. L. Fork et al. "Compression of optical pulses to six femtoseconds by using cubic phase compensation". In: *Opt. Lett.* 12.7 (July 1987), pp. 483–485. DOI: 10.1364/OL.12.000483. URL: https://opg.optica.org/ol/abstract.cfm?URI=ol-12-7-483.

[18] Mette B Gaarde, Jennifer L Tate, and Kenneth J Schafer. "Macroscopic aspects of attosecond pulse generation". In: *Journal of Physics B: Atomic, Molecular and Optical Physics* 41.13 (2008), p. 132001.

[19] Theodor W. Hänsch. "Nobel Lecture: Passion for precision". In: *Rev. Mod. Phys.* 78 (4 Nov. 2006), pp. 1297–1309. DOI: `10.1103/RevModPhys.78.1297`. URL: `https://link.aps.org/doi/10.1103/RevModPhys.78.1297`.

[20] Liran Hareli, Georgiy Shoulga, and Alon Bahabad. "Phase matching and quasi-phase matching of high-order harmonic generation—a tutorial". In: *Journal of Physics B: Atomic, Molecular and Optical Physics* 53 (Dec. 2020), p. 233001. DOI: `10.1088/1361-6455/abb937`.

[21] M. Hentschel et al. "Attosecond metrology". In: *Nature* 414.6863 (2001), pp. 509–513. ISSN: 1476-4687. DOI: `10.1038/35107000`. URL: `https://doi.org/10.1038/35107000`.

[22] Warein Holgado. "Study of high-order harmonic generation effects under variations of focusing conditions of few cycle laser pulses". PhD thesis. Nov. 2016.

[23] Kenichi L. Ishikawa. "High-Harmonic Generation". In: *Advances in Solid State Lasers*. Ed. by Mikhail Grishin. Rijeka: IntechOpen, 2010. Chap. 19. DOI: `10.5772/7961`. URL: `https://doi.org/10.5772/7961`.

[24] J. Itatani et al. "Attosecond Streak Camera". In: *Phys. Rev. Lett.* 88 (17 Apr. 2002), p. 173903. DOI: `10.1103/PhysRevLett.88.173903`. URL: `https://link.aps.org/doi/10.1103/PhysRevLett.88.173903`.

[25] Hossein Z Jooya et al. "Generation of isolated ultra-short attosecond pulses by coherent control of the population of excited states". In: *Physics Letters A* 380.1-2 (2016), pp. 316–321.

[26] D.J. Kane and R. Trebino. "Characterization of arbitrary femtosecond pulses using frequency-resolved optical gating". In: *IEEE Journal of Quantum Electronics* 29.2 (1993), pp. 571–579. DOI: `10.1109/3.199311`.

[27] Leonid V Keldysh. "Ionization in the field of a strong electromagnetic wave". In: *Zh. Eksperim. i Teor. Fiz.* 47 (1964).

[28] Marco Kienel et al. "12 *m*J *k*W-class ultrafast fiber laser system using multidimensional coherent pulse addition". In: *Opt. Lett.* 41.15 (2016), pp. 3343–3346. DOI: 10.1364/OL.41.003343. URL: https://doi.org/10.1364/OL.41.003343.

[29] M. F. Kling et al. "Control of Electron Localization in Molecular Dissociation". In: *Science* 312.5771 (2006), pp. 246–248. DOI: 10.1126/science.1126259. eprint: https://www.science.org/doi/pdf/10.1126/science.1126259. URL: https://www.science.org/doi/abs/10.1126/science.1126259.

[30] K. Klünder et al. "Probing Single-Photon Ionization on the Attosecond Time Scale". In: *Phys. Rev. Lett.* 106 (14 Apr. 2011), p. 143002. DOI: 10.1103/PhysRevLett.106.143002. URL: https://link.aps.org/doi/10.1103/PhysRevLett.106.143002.

[31] Jeffrey L. Krause, Kenneth J. Schafer, and Kenneth C. Kulander. "High-order harmonic generation from atoms and ions in the high intensity regime". In: *Phys. Rev. Lett.* 68 (24 June 1992), pp. 3535–3538. DOI: 10.1103/PhysRevLett.68.3535. URL: https://link.aps.org/doi/10.1103/PhysRevLett.68.3535.

[32] Ferenc Krausz. "The birth of attosecond physics and its coming of age". In: *Physica Scripta* 91.6 (May 2016), p. 063011. DOI: 10.1088/0031-8949/91/6/063011. URL: https://dx.doi.org/10.1088/0031-8949/91/6/063011.

[33] Tadeusz Marek Krygowski and Michał Ksawery Cyrański. "Structural aspects of aromaticity". In: *Chemical Reviews* 101.5 (2001), pp. 1385–1420.

[34] A. L'Huillier, K. J. Schafer, and K. C. Kulander. "Higher-order harmonic generation in xenon at 1064 nm: The role of phase matching". In: *Phys. Rev. Lett.* 66 (17 Apr. 1991), pp. 2200–2203. DOI: 10.1103/PhysRevLett.66.2200. URL: https://link.aps.org/doi/10.1103/PhysRevLett.66.2200.

[35] Anne L'Huillier et al. "Calculations of high-order harmonic-generation processes in xenon at 1064 nm". In: *Phys. Rev. A* 46 (5 Sept. 1992), pp. 2778–2790. DOI: 10.1103/PhysRevA.46.2778. URL: https://link.aps.org/doi/10.1103/PhysRevA.46.2778.

[36]   X. F. Li et al. "Multiple-harmonic generation in rare gases at high laser intensity". In: *Phys. Rev. A* 39 (11 June 1989), pp. 5751–5761. DOI: `10.1103/PhysRevA.39.5751`. URL: `https://link.aps.org/doi/10.1103/PhysRevA.39.5751`.

[37]   F. Lindner et al. "Attosecond Double-Slit Experiment". In: *Phys. Rev. Lett.* 95 (4 July 2005), p. 040401. DOI: `10.1103/PhysRevLett.95.040401`. URL: `https://link.aps.org/doi/10.1103/PhysRevLett.95.040401`.

[38]   L. Lompré et al. "High-order harmonic generation in xenon: intensity and propagation effects". In: *J. Opt. Soc. Am. B* 7.4 (1990), pp. 754–761. DOI: `10.1364/JOSAB.7.000754`.

[39]   D. B. Milošević et al. "Above-threshold ionization by few-cycle pulses". In: *Journal of Physics B: Atomic, Molecular and Optical Physics* 39.14 (2006), R203. DOI: `10.1088/0953-4075/39/14/R01`. URL: `https://dx.doi.org/10.1088/0953-4075/39/14/R01`.

[40]   Bruno Moio et al. "Reconstruction of few-fs XUV pulses with a perturbative approach". In: *EPJ Web of Conferences*. Vol. 255. EDP Sciences. 2021, p. 11008.

[41]   Bruno Moio et al. "Time-frequency mapping of two-colour photoemission driven by harmonic radiation". In: *Journal of Physics B: Atomic, Molecular and Optical Physics* 54.15 (2021), p. 154003.

[42]   P. F. Moulton. "Spectroscopic and laser characteristics of Ti:Al$_2$O$_3$". In: *J. Opt. Soc. Am. B* 3.1 (Jan. 1986), pp. 125–133. DOI: `10.1364/JOSAB.3.000125`. URL: `https://opg.optica.org/josab/abstract.cfm?URI=josab-3-1-125`.

[43]   H. G. Muller. "Reconstruction of attosecond harmonic beating by interference of two-photon transitions". In: *Applied Physics B* 74.1 (June 2002), s17–s21. ISSN: 1432-0649. DOI: `10.1007/s00340-002-0894-8`. URL: `https://doi.org/10.1007/s00340-002-0894-8`.

[44]   M. Nisoli, S. De Silvestri, and O. Svelto. "Generation of high energy 10 fs pulses by a new pulse compression technique". In: *Applied Physics Letters* 68.20 (May 1996), pp. 2793–2795. ISSN: 0003-6951. DOI: `10.1063/1.116609`. eprint:

https://pubs.aip.org/aip/apl/article-pdf/68/20/2793/11812745/2793_1_online.pdf. URL: https://doi.org/10.1063/1.116609.

[45] T. Nubbemeyer et al. "1 kW, 200 mJ picosecond thin-disk laser system". In: *Optics Letters* 42.7 (2017), pp. 1381–1384. DOI: 10.1364/OL.42.001381. URL: https://doi.org/10.1364/OL.42.001381.

[46] P. M. Paul et al. "Observation of a Train of Attosecond Pulses from High Harmonic Generation". In: *Science* 292.5522 (2001), pp. 1689–1692. DOI: 10.1126/science.1059413. eprint: https://www.science.org/doi/pdf/10.1126/science.1059413. URL: https://www.science.org/doi/abs/10.1126/science.1059413.

[47] Luis Plaja, Ricardo Torres, and Amelle Zaïr. "Attosecond physics". In: *Springer Series in Optical Sciences* 177 (2013).

[48] Luca Poletto et al. "Time-delay compensated monochromator for the spectral selection of extreme-ultraviolet high-order laser harmonics". In: *Review of Scientific Instruments* 80.12 (Dec. 2009), p. 123109. ISSN: 0034-6748. DOI: 10.1063/1.3273964. eprint: https://pubs.aip.org/aip/rsi/article-pdf/doi/10.1063/1.3273964/16071150/123109_1_online.pdf. URL: https://doi.org/10.1063/1.3273964.

[49] S Porcinai and Paolo Foggi. "Ab initio calculations of the structure and conformations of 2, 6-lutidine". In: *Nuovo Cimento. D* 19.7 (1997), pp. 889–900.

[50] Michael G Pullen et al. "Kinematically complete measurements of strong field ionization with mid-IR pulses". In: *Journal of Physics B: Atomic, Molecular and Optical Physics* 47.20 (2014), p. 204010. DOI: 10.1088/0953-4075/47/20/204010. URL: https://dx.doi.org/10.1088/0953-4075/47/20/204010.

[51] Xue-jun Qiu et al. "Ultrafast Dynamics Through Conical Intersections in 2, 6-dimethylpyridine Studied with Time-resolved Photoelectron Imaging". In: *Chinese Journal of Chemical Physics* 24.5 (2011), pp. 551–556.

[52] Wolfgang Roebke. "Gas-phase photolysis of 2-picoline". In: *The Journal of Physical Chemistry* 74.24 (1970), pp. 4198–4203.

[53] K. J. Schafer et al. "Above threshold ionization beyond the high harmonic cutoff". In: *Phys. Rev. Lett.* 70 (11 Mar. 1993), pp. 1599–1602. DOI: 10.1103/PhysRevLett.70.1599. URL: https://link.aps.org/doi/10.1103/PhysRevLett.70.1599.

[54] M. Schultze et al. "Delay in Photoemission". In: *Science* 328.5986 (2010), pp. 1658–1662. DOI: 10.1126/science.1189401. eprint: https://www.science.org/doi/pdf/10.1126/science.1189401. URL: https://www.science.org/doi/abs/10.1126/science.1189401.

[55] D. E. Spence, P. N. Kean, and W. Sibbett. "60-fsec pulse generation from a self-mode-locked Ti:sapphire laser". In: *Opt. Lett.* 16.1 (Jan. 1991), pp. 42–44. DOI: 10.1364/OL.16.000042. URL: https://opg.optica.org/ol/abstract.cfm?URI=ol-16-1-42.

[56] Ramesh Srinivasan et al. "Dark structures in molecular radiationless transitions determined by ultrafast diffraction". In: *Science* 307.5709 (2005), pp. 558–563.

[57] Albert Stolow. "Time-resolved photoelectron spectroscopy: Non-adiabatic dynamics in polyatomic molecules". In: *International Reviews in Physical Chemistry* 22.2 (2003), pp. 377–405.

[58] Donna Strickland and Gerard Mourou. "Compression of amplified chirped optical pulses". In: *Optics Communications* 55.6 (1985), pp. 447–449. ISSN: 0030-4018. DOI: 10.1016/0030-4018(85)90151-8. URL: https://www.sciencedirect.com/science/article/pii/0030401885901518.

[59] Noslen Suárez et al. "High-order-harmonic generation in atomic and molecular systems". In: *Physical Review A* 95.3 (2017), p. 033415.

[60] D. Sutter et al. "Semiconductor saturable-absorber mirror–assisted Kerr-lens mode-locked Ti:sapphire laser producing pulses in the two-cycle regime". In: *Opt. Lett.* 24.9 (1999), pp. 631–633. DOI: 10.1364/OL.24.000631.

[61] R. Szipöcs et al. "Chirped multilayer coatings for broadband dispersion control in femtosecond lasers". In: *Opt. Lett.* 19.4 (1994), pp. 201–203. DOI: 10.1364/OL.19.000201.

[62] Naoto Tamai and Hiroshi Miyasaka. "Ultrafast dynamics of photochromic systems". In: *Chemical Reviews* 100.5 (2000), pp. 1875–1890.

[63] H. R. Telle et al. "Carrier-envelope offset phase control: A novel concept for absolute optical frequency measurement and ultrashort pulse generation". In: *Applied Physics B* 69.4 (1999), pp. 327–332. DOI: 10.1007/s003400050813. URL: https://doi.org/10.1007/s003400050813.

[64] M. Uiberacker et al. "Attosecond real-time observation of electron tunnelling in atoms". In: *Nature* 446.7136 (Apr. 2007), pp. 627–632. ISSN: 1476-4687. DOI: 10.1038/nature05648. URL: https://doi.org/10.1038/nature05648.

[65] Giulio Vampa and T Brabec. "Merge of high harmonic generation from gases and solids and its implications for attosecond science". In: *Journal of Physics B: Atomic, Molecular and Optical Physics* 50 (Apr. 2017), p. 083001. DOI: 10.1088/1361-6455/aa528d.

[66] J. Van Houten. "A Century of Chemical Dynamics Traced through the Nobel Prizes. 1967: Eigen, Norrish, and Porter". In: *Journal of Chemical Education* 79.5 (May 2002), p. 548. DOI: 10.1021/ed079p548. URL: https://doi.org/10.1021/ed079p548.

[67] J. Van Houten. "A Century of Chemical Dynamics Traced through the Nobel Prizes. 1999: Ahmed H. Zewail". In: *Journal of Chemical Education* 79.12 (May 2002), p. 1396. DOI: 10.1021/ed079p1396. URL: https://doi.org/10.1021/ed079p1396.

[68] C. Vozzi et al. "Optimal spectral broadening in hollow-fiber compressor systems". In: *Applied Physics B* 80.3 (2005), pp. 285–289. DOI: 10.1007/s00340-004-1721-1. URL: https://doi.org/10.1007/s00340-004-1721-1.

[69] Kenneth E Wilzbach and David J Rausch. "Photochemistry of nitrogen heterocycles. Dewar pyridine and its intermediacy in photoreduction and photohydration of pyridine". In: *Journal of the American Chemical Society* 92.7 (1970), pp. 2178–2179.

[70] L. Xu et al. "Route to phase control of ultrashort light pulses". In: *Opt. Lett.* 21.21 (1996), pp. 2008–2010.

[71] Jie Yang et al. "Simultaneous observation of nuclear and electronic dynamics by ultrafast electron diffraction". In: *Science* 368.6493 (2020), pp. 885–889.

[72] Ahmed H. Zewail. "Femtochemistry: Atomic-Scale Dynamics of the Chemical Bond". In: *The Journal of Physical Chemistry A* 7104.24 (June 2000), pp. 5660–5694. DOI: 10.1021/jp001460h. URL: https://doi.org/10.1021/jp001460h.

[73] Dongping Zhong et al. "Femtosecond dynamics of valence-bond isomers of azines: transition states and conical intersections". In: *Chemical physics letters* 298.1-3 (1998), pp. 129–140.